J. Fluid Mech. (2003), *vol.* 485, *pp.* 279–306. © 2003 Cambridge University Press
DOI: 10.1017/S0022112003004452 Printed in the United Kingdom

Nonlinear steady convection in rotating mushy layers

By D. N. RIAHI

Department of Theoretical and Applied Mechanics, 216 Talbot Laboratory, 104 South Wright Street,
University of Illinois at Urbana-Champaign, Urbana, IL 61801, USA

(Received 28 March 2002 and in revised form 6 December 2002)

We consider the problem of nonlinear steady convection in a horizontal mushy layer rotating about a vertical axis. We analyse the stationary modes of convection in the form of two-dimensional oblique rolls and three-dimensional distorted patterns. Under a near-eutectic approximation and the limit of large far-field temperature, we determine the two- and three-dimensional solutions to the weakly nonlinear problem by using a perturbation technique, and the stability of these solutions is investigated with respect to arbitrary three-dimensional disturbances. The results of the analyses in a particular range of values of the amplitude of convection indicate in particular that, over most of the range of values of the parameters, subcritical convection in the form of down-hexagons with down-flow at the cell centres and up-flow at the cell boundaries can be preferred over up-hexagonal convection, where the convective flow is upward at the cell centres and downward at the cell boundaries. For zero or very small values of $\mathscr{T}$ ($\mathscr{T} \ll 1$), which is the square root of a Taylor number, rolls are preferred over supercritical rectangles, while supercritical rectangles, which are characterized by an angle γ of about 60°, are stable and preferred over the rolls for T above some value. Here, γ or $180^\circ - \gamma$ are the angles between any two adjacent wavenumber vectors of a rectangular cell. For increasing values of T, these rectangles become subcritically unstable and are replaced by new supercritical rectangles of higher γ values, and γ increases with T until supercritical squares ($\gamma = 90^\circ$) become stable. The significance and realizability of down-hexagons, rectangles and squares are found to be due to the interactions between the local solid fraction and the flow associated with the Coriolis term in the momentum–Darcy equation that are fully taken into account in the present study.

1. Introduction

Recently Guba (2001) considered the problem of finite-amplitude steady convection in a horizontal mushy layer rotating about a vertical axis. The investigation was based on the mushy-layer model developed by Amberg & Homsy (1993) and Anderson & Worster (1995) where a near-eutectic approximation was employed in the limit of large far-field temperature. The model allows examination of the dynamics of the mushy layer in the form of a small deviation from the classical system of convection in a horizontal porous layer of constant permeability. Guba (2001) excluded interactions between the local solid fraction and the convection associated with the Coriolis term in the Darcy–momentum equation by fixing the local solid fraction at a constant value in the term modelling the effect of rotation. The goal of Guba was, then, to determine how rotation of the system affects the convection in this relatively simple case in the absence of those interaction effects. In addition, as in the work of Amberg & Homsy (1993), Guba assumed that the amplitude ε of convection is of the same order as the dimensionless thickness δ of the mushy layer. The form of finite-amplitude convection studied by Guba (2001) was that due to either two-dimensional oblique rolls or distorted hexagons. As Guba explained, and more details can be found in Veronis (1959), due to the rotation of the system, the two-dimensional rolls are oblique in the sense that the streamlines of the flow are confined to planes which are at oblique angles to the axes of convection rolls. Similarly, the hexagonal patterns are distorted in the presence of rotation. Guba (2001) found, in particular, that depending on the range of the parameter values, either subcritical or supercritical oblique rolls can exist and the distorted subcritical hexagons can change their form from up-hexagons to down-hexagons for a rotation rate beyond some critical value.

In the present investigation, we extend the problem treated by Guba (2001) by following Anderson & Worster (1995) in assuming a much wider range $\varepsilon \ll \delta$ for the amplitude of convection, taking into account the presence of interactions between the local solid fraction and the convection associated with the Coriolis term in the momentum–Darcy equation and carrying out a stability analysis of the finite-amplitude steady solutions. We found a number of interesting results, some of which sharply differ from those obtained based on a model of the type studied by Guba (2001). The differences between some of the results in the present study and those due to Guba (2001) are discussed in some detail in § 5. To fully appreciate the results of the present study, which is based on a more realistic model, we also carried out some calculations based on a model of the type studied by Guba (2001), and we found, for example, that convection in the form of either rectangles or squares is not stable and, thus, not preferred over the rolls, while in the present model convection in the form of supercritical rectangles or supercritical squares can be stable and preferred over the rolls in a particular range of values of the rotation rate. However, subcritical rectangles or subcritical squares, which can exist in a particular range of values of the rotation rate, are found to be unstable.

Very recently Govender & Vadasz (2002) analysed the problem of two-dimensional weakly nonlinear steady convection in a horizontal mushy layer rotating about a vertical axis. The authors employed a near-eutectic approximation in the limit of large far-field temperature. The momentum–Darcy equation was extended only to include the time derivative and the Coriolis terms. The authors excluded the interactions between the local solid fraction and the flow associated with the Coriolis term by fixing the local solid fraction as a constant value in the term modelling the effect of rotation. Their two-dimensional weakly nonlinear analysis was based on the order δ^0 of the original governing system. The main result of the study was that two-dimensional flow is supercritical.

In regard to the motivation of the present study and the applicability of the results, understanding rotational effects on buoyancy-driven convection in a mushy layer, which is formed adjacent to the crystal interface in an alloy system, are of interest in both engineering and geophysical applications. Understanding the role and effects of the Coriolis force on the dynamics of a possible mushy layer adjacent to the Earth's inner core interface can be important for further understanding the geodynamo. In industrial crystal growth processes it is desirable to impose certain external constraints, such as rotation, in an optimized manner upon the crystallization system, in order to reduce the effects of the induced convection flow, which can lead to micro-defect density in the crystal and, thus, reduce the quality of the crystal produced. Some theoretical results on the effects of rotation about a vertical axis on the flow of melt during alloy solidification and in the absence of a mushy layer (Riahi 1993) indicated conditions under which rotation may stabilize the flow. Computational studies on the effects of rotation about a vertical axis of a horizontal layer on the flow of melt during alloy solidification (Neilson & Incropera 1993) indicated stabilization of vertical plumes and a lack of meandering. The occurrence of undesirable imperfections, which are called freckles, in an alloy crystal, are believed to be due to convection in vertical chimneys, which are developed following the onset of plume convection within the mushy layer. In the present study we are interested in determining the effects of rotation on the onset of plume convection, the tendency for chimney formation and finite-amplitude steady convection states, which occur near the onset of motion.

The following two sections, §§ 2 and 3 deal with the mathematical formulation of the problem and the finite-amplitude analysis. The results of the steady solutions are presented and discussed in § 4, which is followed by the conclusion in § 5.

2. Formulation

We consider a binary alloy melt that is cooled from below and is solidified at a constant speed V_0. Following Amberg & Homsy (1993) and Anderson & Worster (1995), we consider a mushy layer of thickness d adjacent to and above the solidification front to be physically isolated from the overlying liquid and the underlying solid zones. The overlying liquid is assumed to have a composition $C_0 > C_e$ and temperature $T_\infty > T_L(C_0)$ far above the mushy layer, where C_e is the eutectic composition, $T_L(\tilde{C})$ is the liquidus temperature of the alloy and $\tilde{C}$ is the composition. It is then assumed that the horizontal mushy layer is bounded from above and below by rigid and isothermal boundaries. The solidifying system is assumed to be rotating at a constant speed ω about a vertical axis anti-parallel to the gravity vector. We consider the solidifying system in a moving frame of reference $o\tilde{x}\tilde{y}\tilde{z}$, whose origin lies on the solidification front, translating at speed V_0 with the solidification front in the positive $\tilde{z}$-direction and rotating with the speed ω around the $\tilde{z}$-axis.

It should be noted that the mushy layer is assumed to be in local thermodynamic equilibrium and, thus,

$$\tilde{T} = T_L(C_0) + \Gamma(\tilde{C} - C_0),$$

where $\tilde{T}$ is the temperature and Γ is the slope of the liquidus (Anderson & Worster 1995), which is assumed to be constant. The mushy layer can be appropriately treated as a porous layer (Fowler 1985; Worster 1992), where the solid dendrites and the liquid coexist, and Darcy's law is adopted.

Next, we consider the equations for momentum, continuity, heat and solute for the flow of melt in the mushy layer in the moving frame. These equations are non-dimensionalized by using V_0, k/V_0, k/V_0^2, $\beta \Delta C \rho g k/V_0$, ΔC and ΔT as scales for velocity, length, time, pressure, solute and temperature, respectively. Here k is the thermal diffusivity, ρ is a reference (constant) density, $\beta = \beta^* - \Gamma\alpha^*$, where α^* and β^* are the expansion coefficients for the heat and solute, respectively, $\Delta C = C_0 - C_e$, $\Delta T = T_L(C_0) - T_e$ and T_e is the eutectic temperature. The non-dimensional form of the equations for momentum, continuity, temperature and solute concentration in the mushy layer are

$$K(\tilde{\phi})\tilde{\boldsymbol{u}} = -\nabla\tilde{P} - \tilde{R}\tilde{\theta}\boldsymbol{z} + \mathscr{T}\frac{\tilde{\boldsymbol{u}} \times \tilde{\boldsymbol{z}}}{1 - \tilde{\phi}}, \qquad (1a)$$

$$\nabla \cdot \tilde{\boldsymbol{u}} = 0, \qquad (1b)$$

$$\left(\frac{\partial}{\partial \tilde{t}} - \frac{\partial}{\partial \tilde{z}}\right)(\tilde{\theta} - \tilde{S}_t\tilde{\phi}) + \tilde{\boldsymbol{u}}\cdot\nabla\tilde{\theta} = \nabla^2\tilde{\theta}, \tag{1c}$$

$$\left(\frac{\partial}{\partial \tilde{t}} - \frac{\partial}{\partial \tilde{z}}\right)[(1-\tilde{\phi})\theta + C_r\tilde{\phi}] + \tilde{\boldsymbol{u}}\cdot\nabla\tilde{\theta} = 0, \tag{1d}$$

where $\tilde{\boldsymbol{u}} = \tilde{u}\boldsymbol{x} + \tilde{v}\boldsymbol{y} + \tilde{w}\boldsymbol{z}$ is the volume flux vector per unit area, which is also known as the Darcy velocity vector (Nield 1998), $\tilde{u}$ and $\tilde{v}$ are the horizontal components of $\tilde{\boldsymbol{u}}$ along the $\tilde{x}$- and $\tilde{y}$-directions, respectively, $\boldsymbol{x}$ and $\boldsymbol{y}$ are unit vectors along the positive $\tilde{x}$- and $\tilde{y}$-directions, $\tilde{w}$ is the vertical component of $\tilde{\boldsymbol{u}}$ along the $\tilde{z}$-direction, $\boldsymbol{z}$ is a unit vector along the positive $\tilde{z}$-direction, $\tilde{P}$ is the modified pressure, $\tilde{\theta}$ is the non-dimensional composition, or equivalently temperature (Worster 1992), $\tilde{\theta} = [\tilde{T} - T_L(C_0)]/\Delta T = (\tilde{C} - C_0)/\Delta C, \tilde{t}$ is the time variable, $\tilde{\phi}$ the local solid fraction, $\tilde{R} = \beta \Delta C g \Pi(0)/(V_0\nu)$ is the Rayleigh number, $\Pi(0)$ is the reference value at $\tilde{\phi} = 0$ of the permeability $\Pi(\tilde{\phi})$ of the porous medium, which is assumed to be finite (Worster 1992), ν is the kinematic viscosity, g is acceleration due to gravity, $K(\tilde{\phi}) \equiv \Pi(0)/\Pi(\tilde{\phi})$, $S_t = L/(C_L\Delta T)$ is the Stefan number, C_L is the specific heat per unit volume, L is the latent heat of solidification per unit volume, $C_r = (C_s - C_0)/\Delta C$ is a concentration ratio, C_s is the composition of the solid phase forming the dendrites and $T = 2\omega\Pi(0)/\nu$ is the Coriolis parameter, which is the square root of a Taylor number. Equation (1*d*) is based on the limit of sufficiently large value of the Lewis number k/k_s (Worster 1992; Anderson & Worster 1995), where k_s is the solute diffusivity.

The governing equations (1*a*–*d*) are subject to the following boundary conditions (Amberg & Homsy 1993):

$$\tilde{\theta} + 1 = \tilde{w} = 0 \quad \text{at} \quad \tilde{z} = 0, \tag{2a}$$

$$\tilde{\theta} = \tilde{w} = \tilde{\phi} = 0 \quad \text{at} \quad \tilde{z} = \delta, \tag{2b}$$

where $\delta = dV_0/k$ is a growth Péclet number representing the dimensionless depth of the layer.

Following Amberg & Homsy (1993) and Anderson & Worster (1995) in reducing the model asymptotically, we assume the following rescaling in the limit of sufficiently small δ:

$$C_r = C/\delta, \quad \varepsilon \ll \delta \ll 1, \tag{3a}$$

$$(\tilde{x}, \tilde{y}, \tilde{z}) = (x, y, z)\delta, \quad \tilde{t} = \delta^2 t, \quad R^2 = \delta\tilde{R}, \tag{3b}$$

$$\tilde{\theta} = \theta_B(z) + \varepsilon\theta(x, y, z, t), \tag{3c}$$

$$\tilde{\phi} = \phi_B(z) + \varepsilon\phi(x, y, z, t), \tag{3d}$$

$$\tilde{\boldsymbol{u}} = 0 + (\varepsilon R/\delta)\boldsymbol{u}(x, y, z, t), \tag{3e}$$

$$\tilde{P} = RP_B(z) + R\varepsilon P(x, y, z, t), \tag{3f}$$

where C is an order-one quantity as $\delta \to 0$, and the quantities with subscript B are the basic flow variables for the motionless state and are assumed to be a function of z only. The small deviation of each dependent variable from its basic quantity is measured by a perturbation amplitude ε and can vary with respect to spatial and time variables as shown in (3*c*–*f*).

As discussed in Anderson & Worster (1995), the assumption of thin mushy layer ($\delta \ll 1$) is associated with large non-dimensional far-field temperature $\theta_\infty = [T_\infty - T_L(C_0)]/\Delta T \gg 1$, which can occur when the initial $\tilde{C}$ is close to C_e. The assumption of order-one C corresponds to the near-eutectic approximation

(Fowler 1985), which allows one to describe the mushy layer as a porous layer of constant permeability to the leading order.

The rescaling (3*a*–*f*) is then used in (1*a*–*d*) and (2*a*–*b*). This system of equations and boundary conditions admits a motionless basic state, which is steady and horizontally uniform. The basic-state solution is, in terms of the asymptotic expansions for $\delta \ll 1$;

$$\theta_B = (z-1) + \delta(z-z^2)/2 + \dots, \tag{4a}$$

$$\phi_B = \frac{\delta(1-z)}{C} + \delta^2\left[\frac{-(1-z)^2}{C^2} + \frac{z^2-z}{2C}\right] + \dots, \tag{4b}$$

$$P_B = P_0 + R[(z - z^2/2) + \delta(z^2/2 - z^3/3)/2 + \dots], \tag{4c}$$

where P_0 is a constant. Since $\tilde{\phi}$ is expected to be small, according to (4*b*), the following expansion for $K(\tilde{\phi})$ will be implemented later in the governing system:

$$K(\tilde{\phi}) = 1 + K_1\tilde{\phi} + K_2\tilde{\phi}^2 + \dots, \tag{5}$$

where K_1 and K_2 are constants (Amberg & Homsy 1993).

For the analysis to be presented in the next section, it is convenient to use the general representation

$$\boldsymbol{u} = \boldsymbol{\Omega} V + \boldsymbol{E}\psi, \tag{6a}$$

$$\boldsymbol{\Omega} \equiv \nabla \times \nabla \times \boldsymbol{z}, \qquad \boldsymbol{E} \equiv \nabla \times \boldsymbol{z}, \tag{6b}$$

for the divergent-free vector field $\boldsymbol{u}$ (Chandrasekhar 1961). Here V and ψ are the poloidal and toroidal functions for $\boldsymbol{u}$, respectively. Taking the vertical components of the curl and double curl of (1*a*) and using (1*b*) in (1)–(2), we find the following system, which will be analysed in the next section:

$$\begin{aligned}
&\nabla^2[K(\phi_B + \varepsilon\phi)\Delta_2 V] + \frac{\partial}{\partial z}[\boldsymbol{\Omega} V \cdot \nabla K(\phi_B + \varepsilon\phi)] + \frac{\partial}{\partial z}\{[\nabla K(\phi_B + \varepsilon\phi) \times \nabla\psi]\cdot\boldsymbol{z}\}\\
&\quad - R\Delta_2\theta + \mathscr{T}\frac{\partial}{\partial z}\left\{\left[\frac{1}{1-\phi_B-\varepsilon\phi}\right]\Delta_2\psi + \left[\nabla\frac{\partial}{\partial z}V \times \nabla\left(\frac{1}{1-\phi_B-\varepsilon\phi}\right)\right]\cdot\boldsymbol{z}\right.\\
&\quad \left. + \nabla_2\psi\cdot\nabla_2\left(\frac{1}{1-\phi_B-\varepsilon\phi}\right)\right\} = 0,
\end{aligned} \tag{7a}$$

$$\begin{aligned}
&K(\phi_B + \varepsilon\phi)\Delta_2\psi + \left[\nabla\frac{\partial}{\partial z}V \times \nabla K(\phi_B + \varepsilon\phi)\right]\cdot\boldsymbol{z} + \nabla_2\psi\cdot\nabla_2 K(\phi_B + \varepsilon\phi)\\
&\quad - \mathscr{T}\left\{\left[\frac{1}{1-\phi_B-\varepsilon\phi}\right]\Delta_2\frac{\partial}{\partial z}V - \left[\nabla\psi \times \nabla\left(\frac{1}{1-\phi_B-\varepsilon\phi}\right)\right]\cdot\boldsymbol{z}\right.\\
&\quad \left. + \nabla_2\frac{\partial}{\partial z}V\cdot\nabla_2\left[\frac{1}{1-\phi_B-\varepsilon\phi}\right]\right\} = 0,
\end{aligned} \tag{7b}$$

$$\left(\frac{\partial}{\partial t} - \frac{\delta\partial}{\partial z}\right)(-\theta + S_t\phi) + R\left(\frac{\mathrm{d}\theta_B}{\mathrm{d}z}\right)\Delta_2 V + \nabla^2\theta = \varepsilon R(\boldsymbol{\Omega} V + \boldsymbol{E}\psi)\cdot\nabla\theta, \tag{7c}$$

$$\begin{aligned}
&\left(\frac{\partial}{\partial t} - \frac{\partial}{\partial z}\right)[(-1+\phi_B)\theta + \theta_B\phi + \varepsilon\phi\theta - C\phi/\delta]\\
&\quad + R\left(\frac{\mathrm{d}\theta_B}{\mathrm{d}z}\right)\Delta_2 V = \varepsilon R(\boldsymbol{\Omega} V + \boldsymbol{E}\psi)\cdot\nabla\theta,
\end{aligned} \tag{7d}$$

$$\theta = V = 0 \quad \text{at} \quad z = 0, \tag{7e}$$

$$\theta = V = \phi = 0 \quad \text{at} \quad z = 1, \tag{7f}$$

where

$$\Delta_2 \equiv \frac{\partial^2}{\partial x^2} + \frac{\partial^2}{\partial y^2}, \quad \nabla_2 \equiv \left(\frac{\partial}{\partial x}, \frac{\partial}{\partial y} \right).$$

3. Analysis

In this section we seek steady-state solutions of the nonlinear system (7*a*–*f*) by applying a weakly nonlinear analysis, based on a double series expansion in powers of two small parameters for the perturbation quantities, of the type carried out by Busse (1967) and Busse & Riahi (1980). Here the small parameters are δ and ε, which satisfy the condition given in (3*a*). Following Anderson & Worster (1995), we first make a formal asymptotic expansion in ε and then at each order in ε make a formal asymptotic expansion in δ. The appropriate expansions are for the dependent variables of the perturbation system and for R. These expansions are

$$\begin{aligned}(V, \psi, \theta, \phi, R) = {} & [(V_{00} + \delta V_{01} + \dots), (\psi_{00} + \delta \psi_{01} + \dots), (\theta_{00} + \delta \theta_{01} + \dots), \\ & (\phi_{00} + \delta \phi_{01} + \dots), (R_{00} + \delta R_{01} + \dots)] + \varepsilon [(V_{10} + \delta V_{11} + \dots), \\ & (\psi_{10} + \delta \psi_{11} + \dots), (\theta_{10} + \delta \theta_{11} + \dots), (\phi_{10} + \delta \phi_{11} + \dots), \\ & (R_{10} + \delta R_{11} + \dots)] + \varepsilon^2 [(V_{20} + \delta V_{21} + \dots), (\psi_{20} + \delta \psi_{21} + \dots), \\ & (\theta_{20} + \delta \theta_{21} + \dots), (\phi_{20} + \delta \phi_{21} + \dots), (R_{20} + \delta R_{21} + \dots)] + \dots .\end{aligned} \tag{8}$$

3.1. *Linear problem*

Upon inserting (8) into (7*a*–*f*) and disregarding the nonlinear terms, we find the linear problem. At order $\varepsilon^0 \delta^0$ the system (7*a*–*f*) yields the following results:

$$V_{00} = [(\pi^2 + a^2)/(R_{00} a^2)] \sin(\pi z) \sum_{n=-N}^{N} A_n W_n, \tag{9a}$$

$$\psi_{00} = T\pi [(\pi^2 + a^2)/(R_{00} a^2)] \cos(\pi z) \sum_{n=-N}^{N} A_n W_n, \tag{9b}$$

$$\theta_{00} = -\sin(\pi z) \sum_{n=-N}^{N} A_n W_n, \tag{9c}$$

$$\phi_{00} = [-(\pi^2 + a^2)/(C\pi)][1 + \cos(\pi z)] \sum_{n=-N}^{N} A_n W_n, \tag{9d}$$

$$R_{00}^2 = (\pi^2 + a^2)(\pi^2 + a^2 + \pi^2 \mathscr{T}^2)/a^2, \tag{9e}$$

where

$$W_n = \exp(\mathrm{i} \boldsymbol{a}_n \cdot \boldsymbol{r}). \tag{9f}$$

Here i is the pure imaginary number ($\mathrm{i} = \sqrt{-1}$), subscript n takes only non-zero integer values from $-N$ to N, N is a positive integer representing the number of distinct modes, $\boldsymbol{r}$ is the position vector, and the horizontal wavenumber vectors $\boldsymbol{a}_n$ satisfy the properties

$$\boldsymbol{a}_n \cdot \boldsymbol{z} = 0, \quad |\boldsymbol{a}_n| = a, \quad \boldsymbol{a}_{-n} = -\boldsymbol{a}_n. \tag{10}$$

The coefficients A_n are constants and satisfy the conditions

$$\sum_{n=-N}^{N} A_n A_n^* = 1, \quad A_n^* = A_{-n}, \tag{11}$$

where the asterisk indicates the complex conjugate. Minimizing the expression for R_{00} given in (9*e*), with respect to the wavenumber a, we find

$$R_{00c} = \pi[1 + (1 + \mathscr{T}^2)^{0.5}], \tag{12a}$$

$$a_c = \pi(1 + \mathscr{T}^2)^{0.25}. \tag{12b}$$

Here R_{00c} is the minimum value of R_{00} achieved at $a = a_c$. In all the analyses and solutions to follow hereafter, we shall set $R_{00} = R_{00c}$ and $a = a_c$, unless indicated otherwise. It should be noted that equations (9*a–e*) and (12*b*) are exactly the same as those of Guba (2001); the differences between the present work and Guba (2001) begin to appear in the higher correction terms due to the double limit expansion and the interactions between the local solid fraction and the Coriolis force. As the results to be discussed in the next section indicate, some of the presumed order-one coefficients R_{nm} can become too large for $\mathscr{T}$ somewhat bigger that 1, and so the validity of the present model may become questionable for large values of $\mathscr{T}$. Hence, we shall assume by following Guba (2001) that the value of $\mathscr{T}$ can be at most approximately 1. Also, due to the complexity of the present rotating flow investigation, which is amplified by taking into account the local solid fraction interaction with the Coriolis term, we consider a simplifying assumption by following Anderson & Worster (1995) and focusing on a particular limiting case where K_1 is small, of order δ, so that we can write $K_1 = \delta K_c$, where K_c is a constant of order one.

Considering the governing system (7*a–f*) at order $\varepsilon^0\delta^1$, eliminating ψ_{01} between (7*a*) and (7*b*), multiplying the resulting equation by $-V_{00}$, and (7*c*) by θ_{00}, and adding these last two equations, making use of (7*e–f*) and averaging over the mushy layer, we find the condition for the existence of the solutions V_{01} and θ_{01}. This condition yields

$$R_{01} = \left[\frac{\pi^2 T^2(\pi^2 + a^2)}{2Ca^2 R_{00}}\right] - \frac{R_{00} S_t}{2C} \tag{13a}$$

and at the critical onset condition

$$R_{01c} = \frac{1}{2C}\left\{\frac{\pi T^2}{(1 + \mathscr{T}^2)^{0.5}} - \pi[1 + (1 + \mathscr{T}^2)^{0.5}]S_t\right\}. \tag{13b}$$

It should be noted that the first term in curly brackets of equation (13*b*) represents a new result, which modifies the previously obtained result for the $O(\delta)$ correction to the linear Rayleigh number in Guba (2001).

Hence, the critical Rayleigh number R_c for the linear system can be written as

$$R_c = R_{00c} + \delta R_{01c} + O(\delta^2). \tag{14}$$

The solutions at this order can be written in the form

$$(V_{01}, \psi_{01}, \theta_{01}, \phi_{01}) = [V_{01}^*(z), \psi_{01}^*(z), \theta_{01}^*(z), \phi_{01}^*(z)] \sum_{n=-N}^{N} A_n W_n, \tag{15}$$

where the expressions for the coefficients V_{01}^*, ψ_{01}^*, θ_{01}^* and ϕ_{01}^*, which are functions of z and the non-dimensional parameters of the problem, are not given in here. Instead, they are available on request from the author or the Journal of Fluid Mechanics editorial office.

3.2. *Nonlinear problem*

Next, we analyse the nonlinear problem for the steady convection. The solvability conditions for the nonlinear systems require the following special solutions V_{00n} and θ_{00n} of the linear system:

$$(V_{00n}, \theta_{00n}) = \left[\frac{\pi^2 + a^2}{R_{00} a^2},\ -1\right] \sin(\pi z) A_n W_n. \tag{16}$$

It turns out that there is no need to consider special linear solution for ψ and ϕ since the governing nonlinear systems are usually reduced to a form where only (16) will be needed to form the corresponding solvability conditions. Consider the system (7*a–f*) at order ε. Multiplying the equation resulted from eliminating ψ_{10} between (7*a*) and (7*b*) by $-V_{00n}$, (7*c*) by θ_{00n}, adding, applying the boundary conditions (7*e–f*) and averaging over the mushy layer, we find

$$R_{10}|A_n|^2 = -\pi \mathscr{T}^2 \left[\frac{(\pi^2 + a^2)^2}{C R_{00} a^2}\right] \sum_{l,p} (1 + \Phi_{lp}) A_n A_l A_p \langle W_n W_l W_p \rangle, \tag{17a}$$

where

$$\Phi_{lp} = \boldsymbol{a}_l \cdot \boldsymbol{a}_p / a^2, \tag{17b}$$

and an angular bracket indicates the average over the layer. The right-hand side of (17*a*) for R_{10} indicates that $R_{10} = 0$, unless

$$\boldsymbol{a}_n + \boldsymbol{a}_l + \boldsymbol{a}_p = 0 \tag{18}$$

for at least some l and p. The condition (18) can be satisfied in the cases where convection is in the form of either hexagonal or triangular patterns (Busse 1989), while (18) cannot be satisfied for convection in the form of two-dimensional rolls, squares or rectangles. It should also be noted that the existence of triangle-type solution ($N = 3$) is ruled out in the present problem since a pure imaginary value for A_n, which holds in this case (Gorkov 1957), does not satisfy (17*a*). The solutions at this order can be written in the form

$$\begin{aligned}(V_{10}, \psi_{10}, \theta_{10}, \phi_{10}) = {} & [V_{10}^{*}(z), \psi_{10}^{*}(z), \theta_{10}^{*}(z), \phi_{10}^{*}(z)] \sum_{n=-N}^{N} A_n W_n \\ & + \sum_{l,p} [V_{10}^{\wedge}(z, \Phi_{lp}), \psi_{10}^{\wedge}(z, \Phi_{lp}), \theta_{10}^{\wedge}(z, \Phi_{lp}), \phi_{10}^{\wedge}(z, \Phi_{lp})] \sum_{l,p} A_l A_p W_l W_p. \end{aligned} \tag{19}$$

The expressions for V_{10}^{*}, ψ_{10}^{*}, θ_{10}^{*}, ϕ_{10}^{*}, $V_{10}^{\wedge}$, $\psi_{10}^{\wedge}$, $\theta_{10}^{\wedge}$ and $\phi_{10}^{\wedge}$ are not given here.†

We also carry out here the analysis for the system (7*a–f*) at the order $\varepsilon\delta$, mainly because the magnitude of R_{10} due to (17*a*) for the hexagonal patterns is found to be rather small in the range of $\mathscr{T}$ that is considered in the present study. Consider the system (7*a–f*) at the order $\varepsilon\delta$. Multiplying the equation resulting from eliminating ψ_{11} between (7*a*) and (7*b*) by $-V_{00n}$, (7*c*) by θ_{00n}, adding, applying the boundary

---

† Details of these and similar expressions given in this section are available on request from the author or the Journal of Fluid Mechanics Editorial Office, Cambridge.

conditions (7*e–f*) and averaging over the mushy layer, we find

$$R_{11}|A_n|^2=\sum_{l,p}F_{11}(\Phi_{lp})A_nA_lA_p\langle W_nW_lW_p\rangle+G_{11}|A_n|^2, \tag{20}$$

where the expressions for the coefficients F_{11} and G_{11}, which are lengthy, are available on request. As in the case of R_{10}, $R_{11}=0$ unless (18) holds for at least some l and p since the expression for G_{11} is zero for $R_{10}=0$ and the summation term in the right-hand side of (20) vanishes if (18) does not hold. The solutions in this order are quite lengthy and will not be given in this paper.

We now consider the system (7*a–f*) at order ε^2. Multiplying the equation resulting from eliminating ψ_{20} between (7*a*) and (7*b*) by $-V_{00n}$, (7*c*) by θ_{00n}, adding, applying the boundary conditions (7*e–f*) and averaging over the mushy layer, we find

$$\begin{aligned}R_{20}|A_n|^2&=\sum_{l,m,p}F_{20}(\Phi_{lp},\Phi_{ml},\Phi_{mp})A_nA_lA_mA_p\langle W_nW_lW_mW_p\rangle+\sum_{l,p}H_{20}(\Phi_{lp})A_nA_lA_p\\&\quad\times\langle W_nW_lW_p\rangle+G_{20}|A_n|^2\quad(n=-N,\ldots,-1,1,\ldots,N),\end{aligned} \tag{21}$$

where the summations in (21) for l, m and p run from $-N$ to N, and the lengthy expressions for F_{20}, H_{20} and G_{20} are available on request.

The system (21) contains integral expressions of the form $\langle W_nW_lW_p\rangle$, which differ from zero only if (18) is satisfied, and integral expressions of the form $\langle W_nW_lW_mW_p\rangle$, which differ from zero only if

$$\boldsymbol{a}_n+\boldsymbol{a}_l+\boldsymbol{a}_m+\boldsymbol{a}_p=0. \tag{22}$$

The system (21), together with (11), (17*a*) and (20), can be used to study the steady solutions in the form of two-dimensional oblique rolls and three-dimensional distorted cells. We shall restrict our attention to the simplest types of solutions, which include those observed in the applications. These solutions are called regular or semi-regular solutions (Busse 1967). In the case of a regular solution all angles between two neighbouring $\boldsymbol{a}$-vectors are equal and (11) yields

$$|A_1|^2=\ldots=|A_N|^2=\frac{1}{2N}. \tag{23}$$

In the more general semi-regular solution, where (23) still holds, the scalar products between any $\boldsymbol{a}$-vector and its two neighbouring $\boldsymbol{a}$-vectors take the constant values α_1 and α_2. An example of a semi-regular solution is that due to rectangular cells ($N=2$), where $\alpha_1=-\alpha_2$. Regular solutions can follow from the semi-regular ones for the special case $\alpha_1=\alpha_2$. Simple forms of regular solutions correspond to the cases of two-dimensional rolls ($N=1$), square cells ($N=2$) and hexagons ($N=3$).

Thus, using (11), (18) and (22)–(23) in (17*a*), (20) and (21), we find

$$R_{10}=[-\pi T^2(\pi^2+a^2)^2/(CR_{00}a^2\surd 6)]S, \tag{24a}$$

$$R_{11}=[2F_{11}(\Phi_{lp}=0.5)/\surd 6+G_{11}]S, \tag{24b}$$

$$R_{20}=\sum_{m=-N}^{N}T_{nm}|A_m|^2+(2/\surd 6)H_{20}(\Phi_{lp}=0.5)S+G_{20}\qquad(n=-N,\ldots,-1,1,\ldots,N), \tag{24c}$$

where

$$S=\begin{cases}1 & \text{for hexagons}\\ 0 & \text{for non-hexagons,}\end{cases} \tag{24d}$$

$$T_{nm} = F_{-n,n,-n}\delta_{nm} + (F_{n,-n,-n} + F_{-n,-n,n})\delta_{n,-m} + (F_{-m,m,-n} + F_{-n,m,-m} + F_{m,-n,-m})(1-\delta_{nm})(1-\delta_{n,-m}), \quad F_{l,m,p} \equiv F_{20}(\Phi_{lp}, \Phi_{ml}, \Phi_{mp}), \tag{24e}$$

$$\delta_{nm} = \begin{cases} 1 & \text{for} \quad n = m \\ 0 & \text{for} \quad n \neq m. \end{cases} \tag{24f}$$

Here the term 'non-hexagons' in (24*d*) means a solution whose wavenumber vectors do not contain a sub-set of such vectors, which can satisfy a condition of the type (18).

Using (24), the simplest types of solutions, which turn out to be preferred under certain conditions in the present study, are described briefly as follows. For steady two-dimensional oblique rolls,

$$N = 1, \quad A_n = 1/\surd 2, \quad \Phi_{nm} = \pm 1, \quad R_{10} = R_{11} = 0, \quad R_{20} = (T_{11} + T_{1,-1})/2 + G_{20}. \tag{25a}$$

For distorted rectangular (or square) pattern convection,

$$\begin{gathered} N = 2, \; A_n = \tfrac{1}{2}, \; \gamma \leqslant 90^\circ, \quad \Phi_{nm} = \pm 1 \text{ or } \pm\cos\gamma, \\ R_{10} = R_{11} = 0, \quad R_{20} = \tfrac{1}{4}(T_{11} + T_{1,-1} + T_{12} + T_{1,-2}) + G_{20}. \end{gathered} \tag{25b}$$

Here γ is the angle, which does not exceed 90°, between two adjacent wavenumber vectors of any rectangular (or square) cell. For distorted up-hexagonal (down-hexagonal) convection,

$$\begin{gathered} N = 3, \quad A_n = \tfrac{1}{\surd 6}, \quad \Phi = \pm 1 \text{ or } \pm 0.5, \quad R_{10} + \delta R_{11} <(>)\, 0, \\ R_{10} = -\pi T^2 \frac{(\pi^2 + a^2)^2}{C R_{00} a^2 \surd 6}, \quad R_{11} = \frac{F_{11}(\Phi_{lp} = 0.5)}{\surd 6} + G_{11}, \\ R_{20} = \tfrac{1}{6}(T_{11} + T_{1,-1} + T_{12} + T_{1,-2} + T_{13} + T_{1,-3}) + \tfrac{2}{\surd 6} H_{20}(\Phi_{lp} = 0.5) + G_{20}. \end{gathered} \tag{25c}$$

As will be seen later in §4, the sign of the vertical motion at the cell centres for hexagons, which is determined by the sign of ε, can be inferred from the condition

$$\varepsilon(R_{10} + \delta R_{11}) < 0 \tag{26}$$

for the preferred subcritical hexagons. As already indicated, the value of R_{10} in the present problem is found to be rather small for the assumed range of values for $\mathscr{T}$, and, thus, the sign of $(R_{10} + \delta R_{11})$ is taken into account to determine whether hexagons are subcritical or supercritical.

3.3. *Stability problem*

The analysis of the nonlinear steady convection presented in the previous subsection has shown that an infinite manifold of solutions could exist even though this manifold represents only an infinitesimal fraction of the manifold of the solutions (9*a–d*) of the linear problem. To distinguish the physically realizable solution from among all the possible steady solutions, the stability of V, ψ, θ, ϕ with respect to arbitrary three-dimensional disturbances V_d, ψ_d, θ_d, ϕ_d needs to be investigated. The time-dependent disturbances can be assumed to have the form

$$(V_d, \psi_d, \theta_d, \phi_d) = [V'(x,y,z), \psi'(x,y,z), \theta'(x,y,z), \phi'(x,y,z)] \exp(\sigma t), \tag{27}$$

where σ is the growth rate of the disturbances. When the governing equations and the boundary conditions of the form (7*a–f*) for the finite-amplitude steady flow are subtracted from the corresponding equations and boundary conditions for the total dependent variables for the steady flow and the disturbance quantities, and the resulting system is linearized with respect to the disturbance quantities, we obtain the stability system, which is available on request. When the expansion (8) is used in it, it becomes evident that the stability system can be solved by a similar expansion:

$$\begin{aligned}(V', \psi', \theta', \phi', \sigma) = {} & [(V'_{00}+\delta V'_{01}+\ldots), (\psi'_{00}+\delta\psi'_{01}+\ldots), (\theta'_{00}+\delta\theta'_{01}+\ldots),\\ & (\phi'_{00}+\delta\phi'_{01}+\ldots), (\sigma_{00}+\delta\sigma_{01}+\ldots)]+\varepsilon\Bigg[(V'_{10}+\delta V'_{11}+\ldots),\\ & (\psi'_{10}+\delta\psi'_{11}+\ldots), (\theta'_{10}+\delta\theta'_{11}+\ldots), \left(\frac{\phi_{1(-1)}}{\delta}+\phi'_{10}+\delta\phi'_{11}+\ldots\right),\\ & (\sigma_{10}+\delta\sigma_{11}+\ldots)\Bigg]+\varepsilon^2\Bigg[\left(\frac{V_{2(-1)}}{\delta}+V'_{20}+\delta V'_{21}+\ldots\right),\\ & \left(\frac{\psi_{2(-1)}}{\delta}+\psi'_{20}+\delta\psi'_{21}+\ldots\right), \left(\frac{\theta_{2(-1)}}{\delta}+\theta'_{20}+\delta\theta'_{21}+\ldots\right),\\ & \left(\frac{\phi_{2(-1)}}{\delta}+\phi'_{20}+\delta\phi'_{21}+\ldots\right), (\sigma_{20}+\delta\sigma_{21}+\ldots)\Bigg]+\ldots, \end{aligned} \tag{28}$$

where the expansions for ϕ' and all the disturbance variables are singular at order ε and ε^2, respectively, as $\delta \to 0$, but it turns out that such $O(1/\delta)$ terms are needed in the stability analysis since it is found that the stability problems of $O(\varepsilon)$ and $O(\varepsilon^2)$ are forced by terms of order $1/\delta$ in the equations for the disturbances.

For the present stability analysis we restrict ourselves to those disturbances whose dependent variables have wavenumber vectors $\boldsymbol{a}'_n$ which all have the same wavenumber $|\boldsymbol{a}'_n| = a' = a_c$. Then the most critical disturbances, which have the maximum growth rate, are found to be characterized by $\sigma_0 = 0$, where

$$\sigma_0 = \sigma_{00} + \delta\sigma_{01} + \ldots.$$

The linear solutions for the dependent variables of the disturbances at order δ^0 are found to be of the form (9*a–d*), provided A_n, W_n and N are replaced by arbitrary constants $\tilde{A}_n$, $\tilde{W}_n = \exp(\mathrm{i}\boldsymbol{a}'_n \cdot \boldsymbol{r})$ and ∞, respectively.

In analogy with the solvability conditions for the steady motion presented in the previous subsection, the solvability conditions for the disturbance systems at order ε ($n > 1$) require us to define particular solutions of the linear system for the disturbance system. These solutions, designated by $\tilde{V}_{00n}$ and $\tilde{\theta}_{00n}$, have the same form as (15), provided A_n and W_n are replaced, respectively, by $\tilde{A}_n$ and $\tilde{W}_n$. The solvability condition for the disturbance system at order ε is derived similarly to the corresponding one for the steady flow system. We first derived the disturbance system at order ε from the original stability system. Then we eliminated ψ'_{10} in the disturbance system at order ε. Next, applying the solvability condition for the resulting disturbance system at order ε, we found the expression for σ_{10}. Similarly, we applied the solvability conditions at orders $\varepsilon\delta$ and ε^2 to determine σ_{11} and σ_{20}. Since σ_{10}, σ_{11} or σ_{20} may not in general be zero for a particular solution, we define

$$\sigma^* = \varepsilon\sigma_{10} + \varepsilon\delta\sigma_{11} + \varepsilon^2\sigma_{20} \tag{29a}$$

as the leading-order growth rate and combine the solvability conditions at orders ε, $\varepsilon\delta$ and ε^2 to obtain the following system for σ^*:

$$\begin{aligned}(-\sigma^* M + R^*)|\tilde{A}_n|^2 = {} & \sum_{l,p}[\varepsilon L_{10}(\Phi_{lp}, \Psi_{lp}) + \varepsilon\delta L_{11}(\Phi_{lp}, \Psi_{lp}) + \varepsilon^2 L_{20}(\Phi_{lp}, \Psi_{lp})] \\ & \times (\tilde{A}_n \tilde{A}_l A_p \langle \tilde{W}_n \tilde{W}_l W_p \rangle + \tilde{A}_n A_l \tilde{A}_p \langle \tilde{W}_n W_l \tilde{W}_p \rangle) \\ & + \sum_{l,m,p} \varepsilon^2 [F_{20}(\Phi_{lp}, \Phi_{ml}, \Phi_{mp}) + \tilde{F}_{20}(\Phi_{lp})(\Psi_{ml} + \Psi_{mp})] \\ & \times (\tilde{A}_n \tilde{A}_l A_m A_p \langle \tilde{W}_n \tilde{W}_l W_m W_p \rangle + \tilde{A}_n A_l \tilde{A}_m A_p \langle \tilde{W}_n W_l \tilde{W}_m W_p \rangle \\ & + \tilde{A}_n A_l A_m \tilde{A}_p \langle \tilde{W}_n W_l W_m \tilde{W}_p \rangle), \end{aligned} \tag{29b}$$

where

$$R^* = \varepsilon R_{10} + \varepsilon\delta(R_{11} - G_{11}) + \varepsilon^2(R_{20} - G_{20}), \tag{29c}$$

$$\Psi_{lp} = \frac{(\boldsymbol{a}_l \times \boldsymbol{a}_p) \cdot \boldsymbol{z}}{a^2}, \tag{29d}$$

$$M = \frac{R_{00}}{2(\pi^2 + a^2)}, \tag{29e}$$

and the lengthy expressions for $\tilde{F}_{20}$, L_{10}, L_{11} and L_{20} are not given here but are available on request. The growth rates σ^* of the disturbances acting on the finite-amplitude steady motion can then be determined from (29) following the approach due to Busse (1967), which is now a standard stability procedure, for cases where the wavenumber vectors of the disturbances either do or do not coincide with those of the steady motion.

4. Results and discussion

4.1. *Linear problem*

The linear system and its eigenvalue problem, which led to the results (9)–(15), are, in general, functions of the parameters C, S_t and $\mathscr{T}$. Here and thereafter value of $\delta = 0.2$ is chosen to evaluate R_c and other quantities whose values depend on δ. The well-known stabilizing effect of the Coriolis force on convection (Chandrasekhar 1961) can be seen from the expressions for R_c and a_c, (12*a–b*), (13*b*) and (14). Both R_c and a_c increase with $\mathscr{T}$. However, a_c is independent of C and S_t, while R_c depends only weakly on these two parameters. For $\mathscr{T} = 0$, R_c decreases with increasing S_t, for a given C, and increases with C, for a given S_t. Thus, the effects of increasing S_t and C are, respectively, destabilizing and stabilizing at the onset of motion. These results are understandable from the physical interpretation of the parameters S_t and C, since S_t represents a measure of the latent heat relative to the heat content and C represents the difference between the characteristic composition of the solid and liquid phases and the compositional variation of the liquid. However, in the rotating case ($\mathscr{T} \neq 0$) there is a competition between the stabilizing effects of C and $\mathscr{T}$, which depends on the values of S_t and $\mathscr{T}$. Since the dependence of R_c on C and S_t is through the expression for R_{01c} given in (13*b*), we find that for $0 < S_t < S_{tc1}$, where

$$S_{tc1} = \frac{\mathscr{T}^2}{1 + \mathscr{T}^2 + (1 + \mathscr{T}^2)^{0.5}}, \tag{30}$$

then R_c decreases with increasing either C or S_t. For $S_t > S_{tc1}$, then R_c increases with C, while it still decreases with increasing S_t. Figure 1, which presents R_c versus C for

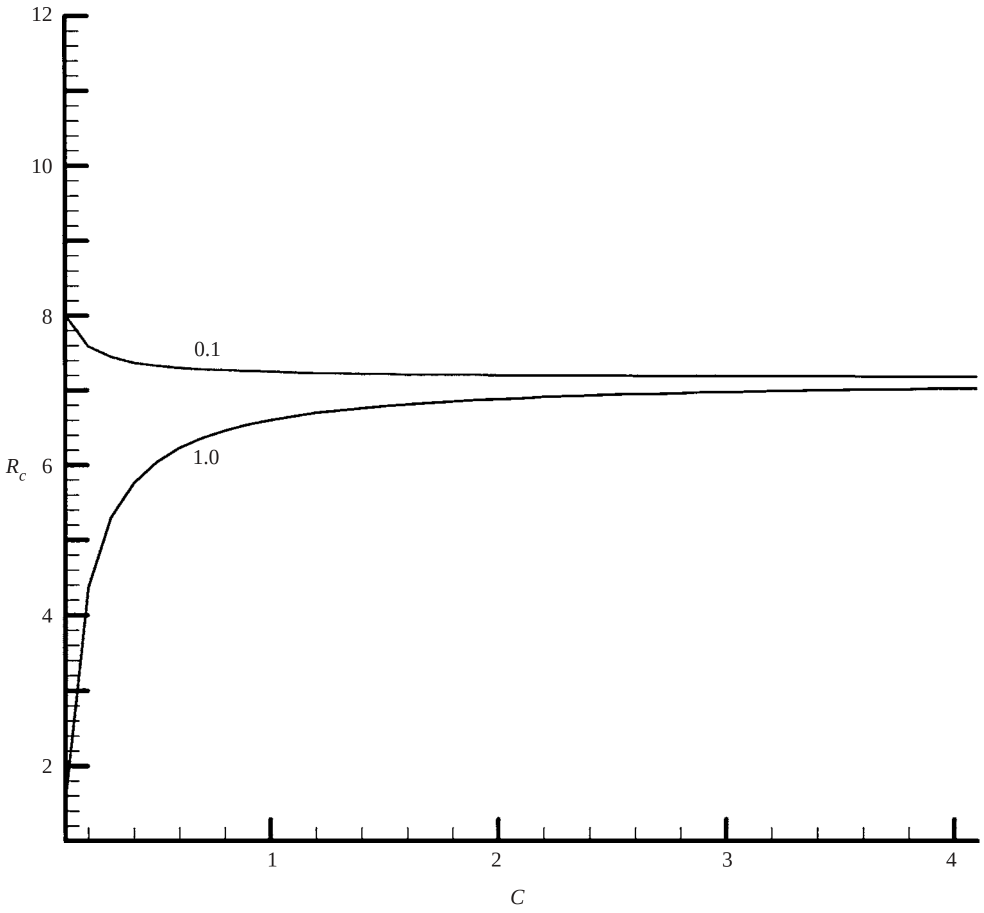

FIGURE 1. R_c against C for $S_t = 0.1$ and 1.0. Here $\mathscr{T} = 0.8$.

$\mathscr{T} = 0.8$ and for two cases $S_t = 0.1$ ($S_t < S_{tc1} = 0.219$) and $S_t = 1.0$ ($S_t > S_{tc1}$), illustrates these results. It can be seen from (30) that S_{tc1} increases with $\mathscr{T}$ and reaches 1 as $\mathscr{T} \rightarrow \infty$. Thus, in a small range for S_t bounded from above by S_{tc1}, the only stabilizing effect is due to $\mathscr{T}$, and both C and S_t are destabilizing in the sense that R_c decreases with increasing either C or S_t. To see the main cause for the destabilizing effect of C when S_t is bounded from above by S_{tc1}, we consider the expression (13*b*) for R_{01c} and note that the first term inside the bracket on the right-hand side, which is independent of S_t, is due to the interaction between the leading term in the basic state of the local solid fraction and the Coriolis term in the momentum–Darcy equation. This interaction term is associated with the basic-state solid fraction because of the difference between the local fluid velocity and the local volume flux of interdendritic fluid, as the momentum equation is formulated in terms of the Darcy, rather than the local, velocity. If this interaction term is not taken into account, then C cannot exhibit the above-described destabilizing effect. We will uncover more surprising results due to the interactions of the local solid fraction with the Coriolis term later in this section.

Due to degeneracy of the linear system, these linear results are applicable to both two- and three-dimensional convection cases, the nonlinear results for which are presented and discussed in the next subsection.

4.2. *Nonlinear problem*

Important quantities due to the nonlinear effects are the coefficients

$$R_1 = R_{10} + \delta R_{11} + O(\delta^2) \tag{31}$$

and R_{20}, which are calculated in the present study. As can be seen from the expansions (8), these coefficients represent leading contributions to the change in R required to obtain finite amplitude ε for a nonlinear solution. In terms of these coefficients the amplitude of convection is of order

$$|\varepsilon| = \frac{|R_1| \pm \left[R_1^2 + 4R_{20}(R - R_c)\right]^{0.5}}{2R_{20}}. \tag{32}$$

There are two expressions for $|\varepsilon|$ corresponding to the plus and minus signs in (32): the plus sign corresponds to the case of maximum $|\varepsilon|$ where R_{20} is positive, while the negative sign corresponds to the case of maximum $|\varepsilon|$ where R_{20} is negative. It should also be noted that for non-zero R_1, which can correspond to convection in the form of hexagons, then the expression (32) for $|\varepsilon|$ is provided only for the subcritical convection state where $R < R_c$, since it is preferred over the supercritical convection in the sense that it generally corresponds to the smallest value of R. In this case the amplitude of convection is largest when the magnitude of R_1 is largest. For $R_1 = 0$, which can correspond to two-dimensional rolls, rectangles and square pattern convection, then the sign of R_{20} determines whether the steady solution exists for values of R above or below R_c. For $R_1 = 0$ and supercritical convection, where $R > R_c$, the amplitude of convection is largest, provided the value of R_{20} is smallest among all the solutions to the nonlinear problem. In the present problem the coefficients R_1 and R_{20} are due to the linear and nonlinear interactions between the local solid fraction and the Coriolis term in the momentum–Darcy equation, the nonlinear convective terms in the temperature equation and the nonlinear interactions between the flow velocity and the non-uniform and nonlinear permeability associated with the perturbation to the basic-state solid fraction.

Hexagonal convection

The coefficient R_1, given by (24*a–b*) and (31), for the hexagonal convection was computed for various values of $\mathscr{T}$, C, S_t, K_c and K_2. It was found that depending on the values of the parameters, R_1 can be either positive or negative, and, thus, the steady hexagonal convection can be supercritical for

$$\varepsilon R_1 > 0 \tag{33a}$$

and subcritical for

$$\varepsilon R_1 < 0. \tag{33b}$$

For the supercritical case, up-hexagons correspond to the region in the (R_1, ε)-plane where $R_1 > 0$ and $\varepsilon > 0$, while down-hexagons correspond to the region where $R_1 < 0$ and $\varepsilon < 0$. For the subcritical case, up-hexagons correspond to the region in the (R_1, ε)-plane where $R_1 < 0$ and $\varepsilon > 0$, while down-hexagons correspond to the region where $R_1 > 0$ and $\varepsilon < 0$.

Some typical results on the effects of $\mathscr{T}$ and K_c are presented in figure 2 for R_1 versus $\mathscr{T}$ for $S_t = 5.0$, $C = 1.0$, $K_2 = 0$, and several values of K_c. It is seen from this

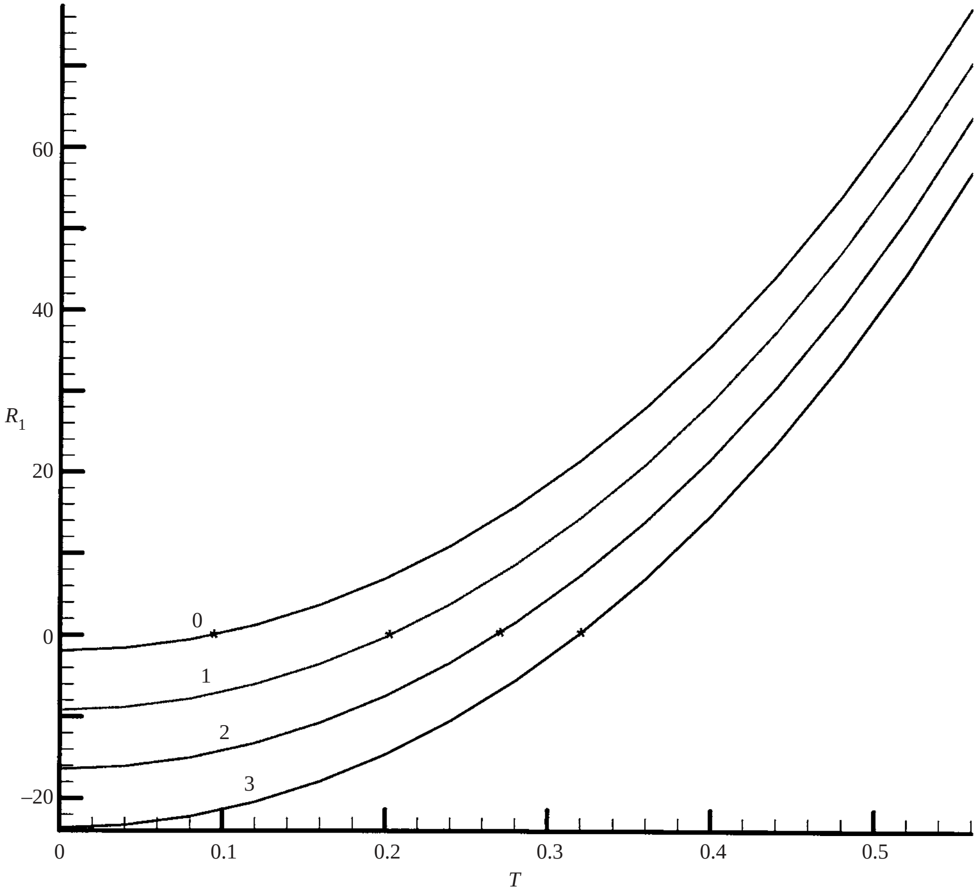

FIGURE 2. R_1 against $\mathscr{T}$ for hexagons. Here $S_t = 5.0$, $C = 1.0$, $K_2 = 0$ and $K_c = 0$, 1.0, 2.0 and 3.0. $\mathscr{T} = \mathscr{T}_{c1}$ is indicated by $*$ on each curve.

figure that for $R_1 < 0$ ($R_1 > 0$), $|R_1|$ decreases (increases) with either increasing $\mathscr{T}$ or decreasing K_c.

The results provided above indicate that the value of R_1 becomes more positive as $\mathscr{T}$ increases or K_c decreases. Hence, preference is given to the down-hexagon if $R_1 > 0$ because under such a situation the down-hexagon is subcritical. Conversely, the tendency for the preference of up-hexagons decreases with increasing $\mathscr{T}$ and increases with K_c. Our additional data indicated that R_1 is negative for $\mathscr{T} = 0$, which agrees with the result due to Amberg & Homsy (1993), but for $\mathscr{T} \neq 0$, R_1 increases with $\mathscr{T}$ until it becomes zero at a critical $\mathscr{T}_{c1}$ of $\mathscr{T}$, beyond which R_1 is positive and generally increases rather rapidly with $\mathscr{T}$. This result was one of the main reasons to restrict the present investigation to small, at most about 1, values of $\mathscr{T}$. For larger values of $\mathscr{T}$, the values of $|R_1|$ become very large, which can invalidate the basic assumption for the expansions of type (8) for the present model. Figures 3 and 4 present the transitional boundary between the subcritical and supercritical hexagons in the $(C, \mathscr{T})$- and $(S_t, \mathscr{T})$-planes for $K_2 = 0$ and for several values of K_c, respectively. In figure 3, S_t is set at fixed value of 1, while in figure 4, C is set at fixed value of 1. The region below each graph in these figures corresponds to $R_1 < 0$, while the region above each graph corresponds to $R_1 > 0$. It can be seen from these figures that

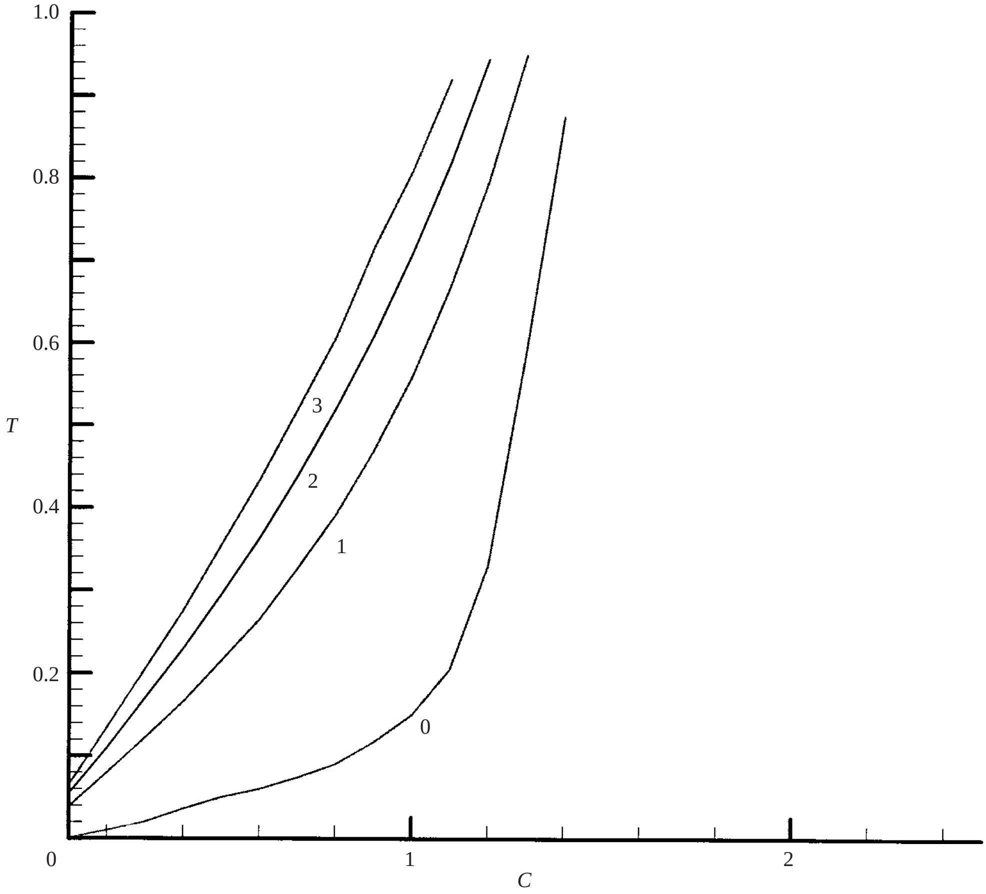

FIGURE 3. Transitional boundary between subcritical and supercritical regimes for hexagons in the $(C, \mathscr{T})$-plane for $K_c = 0$, 1.0, 2.0 and 3.0. Here $S_t = 1.0$ and $K_2 = 0$.

the value of $\mathscr{T}_{c1}$ increases with increasing C or K_c and decreases with increasing S_t. In addition to the effect of the scaled linear measure of the permeability variations K_c, our data indicated that the effect of a nonlinear measure of the permeability variations, K_2, is also to favour up-hexagons in the sense that $|R_1|$ increases with K_2 when $R_1 < 0$ and decreases with increasing K_2 when $R_1 > 0$.

Our data on variations of R_1 with respect $\mathscr{T}$, K_c, C and S_t, together with the results presented in figure 3 indicate that for $\mathscr{T} = 0$, R_1 is negative, $|R_1|$ is small, and the effect of C is stabilizing in the sense that the subcritical effect is reduced with increasing C. For $T \neq 0$ and above T_{c1}, R_1, which is large for small values of C, decreases rather rapidly with increasing C until R_1 becomes zero at some critical C_c of C. For $C > C_c$, R_1 is negative and $|R_1|$ increases slowly with C. The value of C_c increases with $\mathscr{T}$. Hence, in the rotating case for $\mathscr{T} > \mathscr{T}_{c1}$, down-hexagons are preferred over up-hexagons and the effect of C is stabilizing for $C < C_c$, while up-hexagons are preferred over down-hexagons and the effect of C is destabilizing for $C > C_c$. It can be seen from our extensive data and from the figure 4 that for $\mathscr{T} = 0$, R_1 is negative, $|R_1|$ is small, and the effect of S_t is destabilizing in the sense that the subcritical effect is increased with increasing S_t. It turns out that for $\mathscr{T} \neq 0$ and below T_{c1}, R_1 is negative for small S_t and $|R_1|$ decreases with increasing S_t until

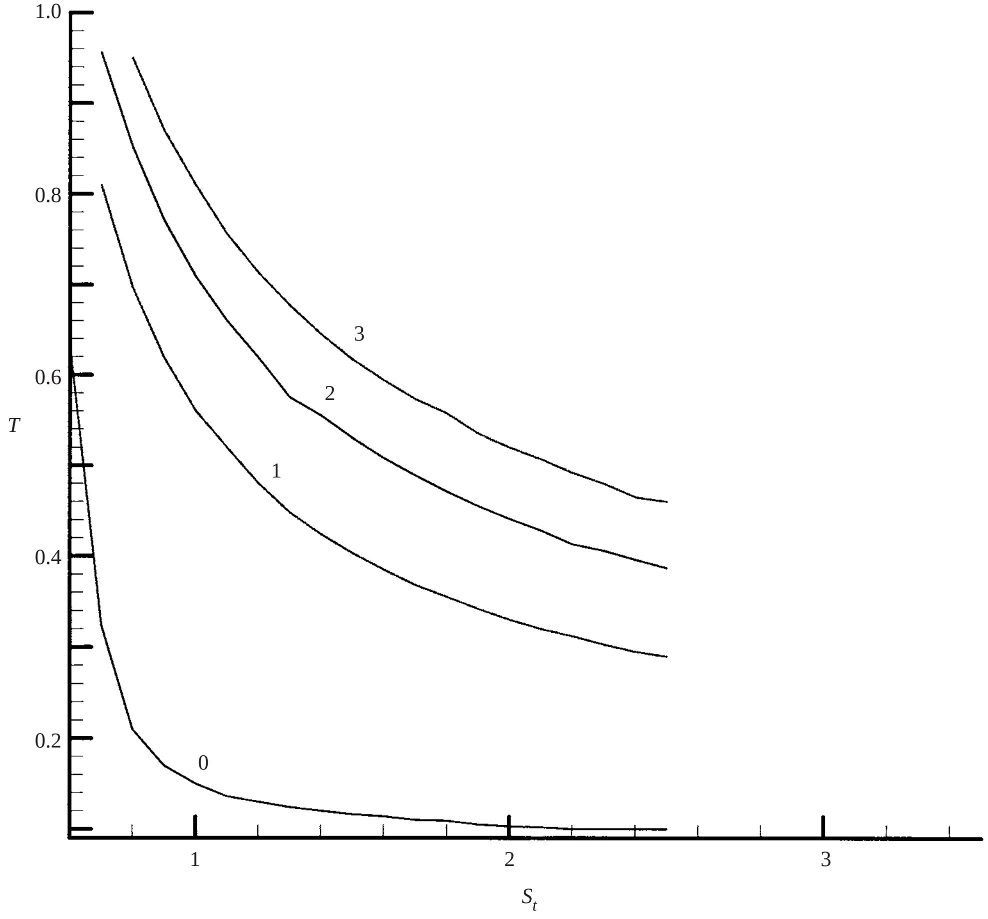

FIGURE 4. Transitional boundary between subcritical and supercritical regimes for hexagons in the $(S_t, \mathscr{T})$-plane for $K_c = 0$, 1.0, 2.0 and 3.0. Here $C = 1.0$ and $K_2 = 0$.

R_1 becomes zero at some critical S_{tc2} of S_t. For $S_t > S_{tc2}$, R_1 is positive and increases with S_t. The value of S_{tc2} decreases with increasing $\mathscr{T}$. For $\mathscr{T} \neq 0$ and above $\mathscr{T}_{c1}$, R_1, which is now positive, increases with S_t. The rate of increase of R_1 with respect of S_t in found to increase with $\mathscr{T}$. Hence, in contrast to the non-rotating case, the tendency for the flow towards the preference of down-hexagons increases with S_t in the range $S_t < S_{tc2}$, while down-hexagons, which are preferred over up-hexagons in the range $S_t > S_{tc2}$, become increasingly more significant as S_t increases beyond S_{tc2}.

Referring to (31), it should be noted that R_{10}, which is entirely due to the interactions between the local solid fraction and the Coriolis term in the momentum-Darcy equation, is zero for $\mathscr{T} = 0$ and negative for $\mathscr{T} \neq 0$, and $|R_{10}|$ increases rapidly with $\mathscr{T}$. However, R_{11}, which is due to these interactions as well as to other nonlinear interactions in the equations, can be either positive or negative depending on the parameter values.

However, if the interactions between the local solid fraction and the Coriolis terms are not taken into account, then it was found that $R_{11} < 0$ for $\mathscr{T}$ below some critical value $\mathscr{T}_{c2}$, where $R_1 < 0$, and $|R_1|$ decreases with increasing $\mathscr{T}$ until R_1 becomes zero at some value of $\mathscr{T} = \mathscr{T}_{c2}$ and then increases with further increases in $\mathscr{T}$. The value

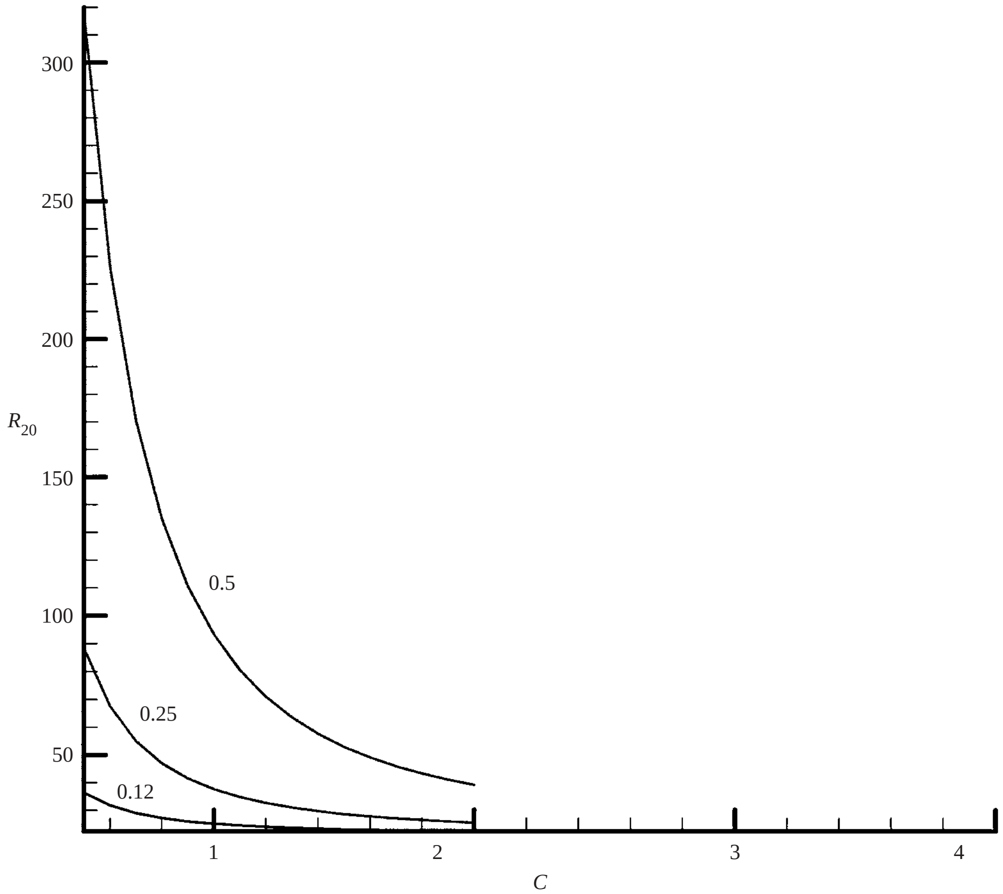

FIGURE 5. R_{20} against C for hexagons. Here $S_t = 1.0$, $K_2 = 0$, and $\mathscr{T} = 0.12$, 0.25 and 0.50.

of $\mathscr{T}_{c2}$ is found to be typically about one order of magnitude larger than the corresponding value for $\mathscr{T}_{c1}$, and $\mathscr{T}_{c2}$ is found to increase with either C or S_t. Some typical values for $\mathscr{T}_{c2}$ are 2.6 and 2.7 ($K_c = 3.0$, $K_2 = 0$, $S_t = 1.0$) for $C = 1.0$ and 2.0, respectively, and $\mathscr{T}_{c2} = 2.6$ and 2.8 ($K_c = 3.0$, $K_2 = 0$, $C = 1.0$) for $S_t = 1.0$ and 5.0, respectively.

The coefficient R_{20}, given by (24*c*), for hexagonal convection ($N = 3$, $A_n = 1/\sqrt{6}$), designated here by $R_{20}^{(h)}$, was computed for various values of $\mathscr{T}$, S_t, C, K_c and K_2. It was found that $R_{20}^{(h)}$ is always positive for both rotating and non-rotating cases. For $\mathscr{T} = 0$, it is independent of C, S_t and K_c, but it increases with K_2. For $\mathscr{T} \neq 0$, $R_{20}^{(h)}$ is independent of S_t and K_c, increases with K_2 and $\mathscr{T}$, and decreases with increasing C. Some typical results on the variation of $R_{20}^{(h)}$ with respect to C for $\mathscr{T} = 0.12$, 0.25 and 0.50 are presented in figure 5 for $K_2 = 0$. It is seen from this figure that the rate of decrease of $R_{20}^{(h)}$ with respect to C is rather high for small C, and $R_{20}^{(h)}$ increases rapidly with $\mathscr{T}$. If the interactions between the local solid fraction and the Coriolis term are not taken into account, then it was found that $R_{20}^{(h)}$ is still positive, independent of C, S_t and K_c, and it increases with K_2 and $\mathscr{T}$. However, its value and its rate of increase with respect to T are rather small if such interactions are not taken into account. Although variations of R_1 with respect to different parameters provide information about various destabilizing and stabilizing features in the rotating case for hexagonal convection, as discussed in the previous two paragraphs, it should be noted that information about R_{20} for hexagons is useful since R_{20} is the leading second-order coefficient in the expansion for R in powers of ε, so $R_{20}^{(h)}$ plays a useful role in calculating the solute flux and the order of magnitude of ε in (32) and in cases where R_1 becomes negligible or for the consideration of the stability hexagons, which will be discussed further in the next subsection.

We also examined the vertical distribution of solid fraction at different locations in the horizontal direction for the hexagonal convection. Our data at the centres and the nodes of hexagons indicated that the perturbation to solid fraction at the nodes is generally positive, while that at the centres is generally negative. This general result holds irrespective of the parameter values considered, which indicates tendency for chimney formation at the cell centres and not at the nodes, contrary to the result of the experiment conducted by Tait, Jahrling & Jaupart (1992) in the absence of rotation. However, it should be noted that neither the present type of model, nor all the linear and weakly nonlinear models developed so far, has made any prediction about presence of chimneys but only predicted the presence some regions of reduced local solid fraction, whereas chimneys were actually observed to form at the nodes of the hexagons in the experiments (Tait *et al.* 1992). The reason for this apparent inconsistency about the locations for the tendency for chimney formation is not known at present, but it could be due to factors such as the intrinsic time-dependent nature of the experiments or due to assumptions in the theory such as the near-eutectic approximation, the large-far-field temperature limit and the prescribed constrained growth at constant solidification rate. In addition, our results indicate that the rotational effect may be beneficial since the perturbation to the solid fraction at any node in the rotating system is found to be greater at any vertical level than in the absence of rotation. Some typical results are presented in figure 6 for the vertical distribution of the basic state and total solid fraction at the centre of a hexagon for $\mathscr{T}=0$ and 0.5. In these calculations $\delta=0.2$, $S_t=C=1.0$, $K_c=K_2=0$, and the value $\varepsilon=0.002$ is chosen, which is the maximum value of ε beyond which the solid fraction becomes negative. This is based on the physical grounds that the deviation of the total solid fraction $\tilde{\phi}$ from ϕ_B cannot be such that $\tilde{\phi}$ becomes negative. We have chosen zero values for K_c and K_2 in these calculations since $\tilde{\phi}$ is found to be much less sensitive to K_c and K_2 at such small value of ε. It is seen from this figure that the solid fraction in the rotating case is notably smaller than that in the absence of rotation, except close to the upper boundary and, hence, the tendency for chimney formation at the cell centres increases in the presence of rotation. The results also indicate that the tendency for chimney formation is higher near the lower boundary than anywhere else in the layer.

Square pattern convection

We now present and discuss the results for another three-dimensional case of convection, in the form of square cells, which, as is discussed later, could become preferred in the present problem for $\mathscr{T}$ in a particular range of values. First, refer back to figure 6, which provides graphs for the total solid fraction at the centre of a square cell in square pattern convection. The parameters are as in the case of hexagons. Again, the tendency for chimney formation increases in the presence of rotation and such tendency is stronger near the lower boundary. It is also seen from this figure that the tendency for chimney formation at the squares-cell centres is apparently higher than that at the hexagons-cell centres. Our additional data at the boundary points between two square cells indicated that the perturbation to the solid

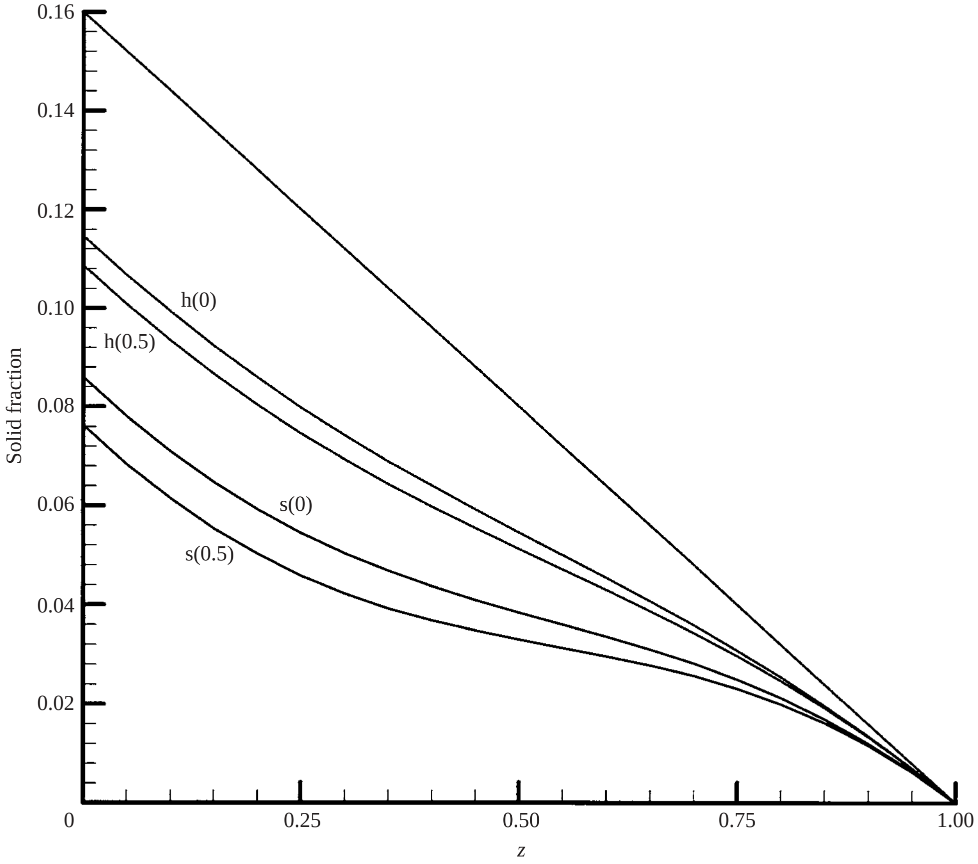

FIGURE 6. Solid fraction for hexagons and squares versus z for $S_t = 1.0$, $C = 1.0$, $K_c = 0$, $K_2 = 0$ and $x = y = 0$. The upper graph presents ϕ_B, while the other graphs present $\tilde{\phi}$ for hexagons (h) and squares (s) at $\mathscr{T} = 0$ and 0.50.

fraction is negative and the tendency for chimney formation is higher in the presence of rotation.

As was explained in the previous section, R_1 is zero for the case where convection is in the form of square cells, and thus we next present and discuss the results for the coefficient R_{20}, given by (24*c*), for square cells ($N = 2$, $A_n = 1/2$), which is designated here by $R_{20}^{(s)}$. This coefficient was computed for various values of $\mathscr{T}$, S_t, C, K_c and K_2. It was found that, depending on the value of $\mathscr{T}$, $R_{20}^{(s)}$ can be positive or negative and thus both supercitical and subcritical squares are possible. Also, $R_{20}^{(s)} < R_{20}^{(h)}$ for both rotating and non-rotating cases. For $\mathscr{T} = 0$, $R_{20}^{(s)}$ is positive and independent of C, S_t and K_c, but it increases with K_2, which is consistent with the stabilizing effect of decreasing the permeability. For $\mathscr{T} \neq 0$, $R_{20}^{(s)}$ is independent of S_t and K_c, increases with K_2, increases initially with $\mathscr{T}$, and decreases with increasing C. Thus, the rotational constraint changes the role of C in the nonlinear regime for squares. As in the case of $R_{20}^{(h)}$, it was found that the rate of decrease of $R_{20}^{(s)}$ with respect to C is high for small C, and $R_{20}^{(s)}$ increases rapidly with $\mathscr{T}$. The square pattern convection is supercritical for sufficiently small values of $\mathscr{T}$. If the interactions between the local solid fraction and the Coriolis term are not taken into account, then the qualitative features of $R_{20}^{(s)}$ are similar to those of $R_{20}^{(h)}$ described before.

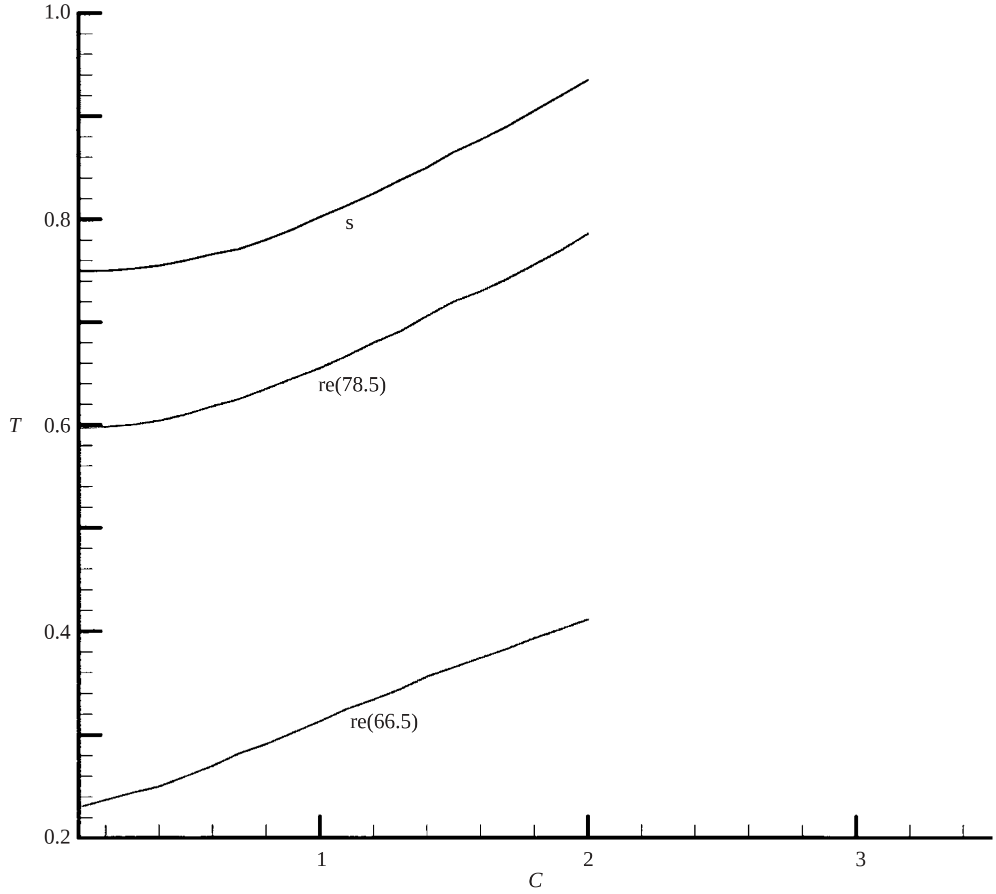

FIGURE 7. Transition boundary between subcritical and supercritical regimes for squares (s) and rectangles (re) with $\gamma = 78.5$ and 66.5 in the $(C, \mathscr{T})$-plane. Here $K_2 = 0$.

We also obtained some results on the variation of $R_{20}^{(s)}$ with $\mathscr{T}$ for different values of C. It was found from our calculated data that $R_{20}^{(s)}$ is positive for sufficiently small $\mathscr{T}$ and increases with $\mathscr{T}$ until reaching a maximum value at some critical $\mathscr{T} = \mathscr{T}_{c3}$. For $\mathscr{T} > \mathscr{T}_{c3}$, $R_{20}^{(s)}$ decreases with increasing $\mathscr{T}$ until $R_{20}^{(s)}$ becomes zero at some critical $\mathscr{T} = \mathscr{T}_{c4}$. For $\mathscr{T} > \mathscr{T}_{c4}$, squares are subcritical. The critical values for $\mathscr{T}_{c3}$ and $\mathscr{T}_{c4}$ are found to increase with C but are independent of K_c and S_t. Some typical values of $\mathscr{T}_{c3}$ are 0.51 and 0.51 ($K_2 = 0$) for $C = 1.0$ and 2.0, respectively. Typical results for $\mathscr{T}_{c4}$ are presented in figure 7, which provides the transition boundary between subcritical and supercritical regimes for squares and for two different rectangles in the $(C, \mathscr{T})$-plane for a fixed value of $K_2 = 0$. Square pattern convection is supercritical in the region below the curve for squares (s) shown in figure 7, and subcritical in the region above the curve. In the subcritical regime, $R_{20}^{(s)}$ increases with C. These qualitative features of squares are found to be entirely due to the interactions between the local solid fraction and the Coriolis term.

Rectangular pattern convection

The simplest semi-regular solutions in the form of different types of rectangular patterns are found to become preferred in the present problem for $\mathscr{T}$ above $\mathscr{T}_{c5}$.

Like to the case of squares, R_1 is zero for rectangles. For T just above the smallest value of $\mathscr{T}_{c5}$, which is very slightly above zero, rectangles with angle γ of about 60° are supercritical and their R_{20} value, which is designated for a general rectangle by $R_{20}^{(re)}$, is smaller than the corresponding values for rolls and rectangles with γ larger than 60°, which includes squares. The critical $\mathscr{T}_{c5}$ is independent of K_c and S_t, and a typical value of $\mathscr{T}_{c5}$ is 0.008 at $K_2 = 0$ and $C = 1.0$. As is discussed later, there is an interesting pattern transitional phenomenon in the sense that γ increases continuously with $\mathscr{T}$ until it reaches 90° and the rectangles become squares. Each such rectangular-cell solutions is found to have the smallest value of $R_{20}^{(re)}$ over some interval in $\mathscr{T}$ in the domain $60° < \gamma < 90°$.

The qualitative results on the total solid fraction for the rectangles are found to be generally similar to those for squares presented and discussed above. The coefficient $R_{20}^{(re)}$, which is independent of K_c and S_t, was computed for various values of $\mathscr{T}$, C, γ and K_2. It was found to be positive for $\mathscr{T}$ below some critical value $\mathscr{T}_{c6}$ and negative for $\mathscr{T}$ above $\mathscr{T}_{c6}$. The critical $\mathscr{T}_{c6}$ is independent of K_c and S_t but increases with γ. Some typical result on the values for $\mathscr{T}_{c6}$ are given in the figure 7, which includes the transition boundary between the subcritical and supercritical rectangles for $\gamma = 66.7°$ and 78.5° in the $(C, \mathscr{T})$-plane. The rectangles are supercritical in the region below the transition curve and subcritical above it. Consistent with the results presented in figure 7, $\mathscr{T}_{c6}$ is found to increase with C and γ. Thus both supercritical and subcritical rectangles can exist in particular range of values of $\mathscr{T}$. As in the case of squares, it was found that $R_{20}^{(re)} < R_{20}^{(h)}$. Qualitative variations of $R_{20}^{(re)}$ with C and K_2 are found to be similar to those for squares. Some typical results on the variations of R_{20} with $\mathscr{T}$ and γ are shown in figure 8 for $C = 1.0$. It can be seen from this figure that the effect of increasing $\mathscr{T}$ is very slightly stabilizing for the supercritical rectangles at lower values of $\mathscr{T}$ and significantly destabilizing for higher values of $\mathscr{T}$. The effect of increasing $\mathscr{T}$ is generally destabilizing for subcritical rectangles. The effect of increasing γ is stabilizing for rectangles.

Two-dimensional rolls

As explained in the previous section, R_1 is zero for two-dimensional rolls. Thus, the important coefficient for rolls ($N = 1$, $A_n = 1/\sqrt{2}$) is R_{20} given in (24*c*), which is designated here by $R_{20}^{(r)}$. This coefficient was computed for various values of $\mathscr{T}$, S_t, C, K_c and K_2. It was found that $R_{20}^{(r)}$ is always positive and thus such flow is supercritical. Also, $R_{20}^{(r)} < R_{20}^{(h)}$ for both rotating and non-rotating cases. However, as can be seen from figure 8, $R_{20}^{(r)}$ is smaller than $R_{20}^{(re)}$ for $\mathscr{T}$ below some critical value $\mathscr{T}_{c7}$, and $R_{20}^{(r)} > R_{20}^{(re)}$ for $\mathscr{T} > \mathscr{T}_{c7}$. The value of $\mathscr{T}_{c7}$ increases with either γ or C but is independent of K_c and S_t. Some typical values of $\mathscr{T}_{c7}$ are 0.15 and 0.35 ($K = 0$, $C = 1.0$) for $\gamma = 64.6°$ and 78.5°, respectively. For $\mathscr{T} = 0$, $R_{20}^{(r)}$ is independent of C, S_t and K_c, but it increases with K_2. For $\mathscr{T} \neq 0$, $R_{20}^{(r)}$ is independent of S_t and K_c, increases with K_2 and $\mathscr{T}$, and decreases with increasing C. Calculations on the variation of $R_{20}^{(r)}$ with C for different values of $\mathscr{T}$ indicated that the rate of decrease of $R_{20}^{(r)}$ with C is high for small C, and $R_{20}^{(r)}$ increases rapidly with $\mathscr{T}$. If the interactions between the local solid fraction and the Coriolis term are excluded from the present model, then qualitatively $R_{20}^{(r)}$ is similar to $R_{20}^{(h)}$ described before.

Figure 9 presents some typical results on comparison between the variation of the coefficient R_{20} with $\mathscr{T}$ for rolls, squares and hexagons. The results are for $C = 1.0$ and $K_2 = 0$. It can be seen from this figure that rolls can be realized at a lower value of the Rayleigh number than squares for $\mathscr{T} < \mathscr{T}_{c7}$, while squares can be realized at

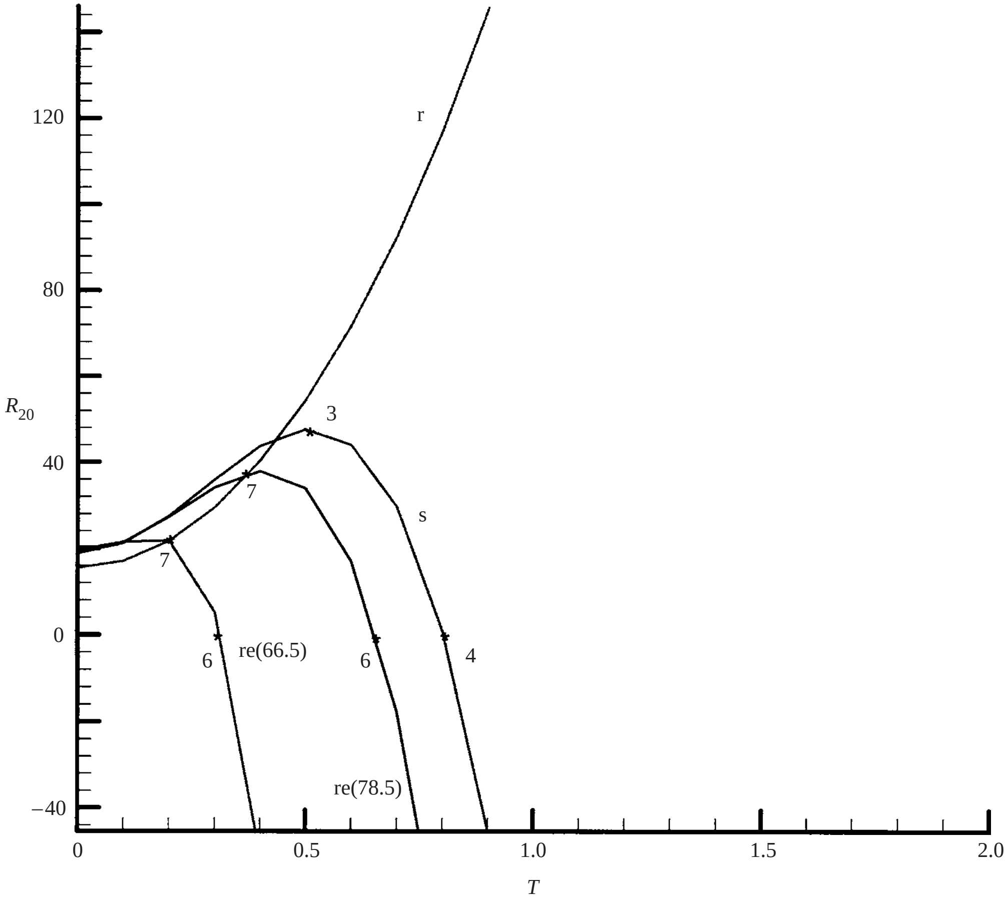

FIGURE 8. R_{20} against $\mathscr{T}$ for rolls (r), squares (s) and rectangles (re) with $\gamma = 78.5°$ and $66.5°$. Here $S_t = 1.0$, $C = 1.0$ and $K_2 = 0$. The locations $\mathscr{T} = \mathscr{T}_{c3}$, $\mathscr{T}_{c4}$, $\mathscr{T}_{c6}$ and $\mathscr{T}_{c7}$ are labelled 3, 4, 6 and 7, respectively.

a lower value of R for $\mathscr{T} > \mathscr{T}_{c7}$. In addition, supercritical hexagons are generally realized at a value of R larger than those due to rolls and squares.

Our calculations for the vertical distribution of the solid fraction at locations between two rolls or at the centres of rolls indicated that the perturbation to the solid fraction at the centres of rolls can be positive, while that at locations between two rolls is generally negative. Hence, there is a greater tendency for chimney formation at locations between the rolls. In addition, it was found that the tendency for chimney formation increases slightly in the presence of rotation, and is significantly higher in a region near the lower boundary.

4.3. *Stability of finite-amplitude steady solutions*

Following standard stability procedures (Schluter, Lortz & Busse 1965; Busse 1967), the system (28*b*) for the growth rate σ^* of disturbances acting on the finite-amplitude steady solutions has been simplified, and the expression for σ^* has been computed for different integers N and various values of Φ_{nm} ($|\Phi_{nm}| \leqslant 1$) and Ψ_{nm} ($|\Psi_{nm}| \leqslant 1$). In all the cases that have been investigated only steady supercritical solutions in the form of rolls, rectangles and squares, and subcritical steady solutions in the form of

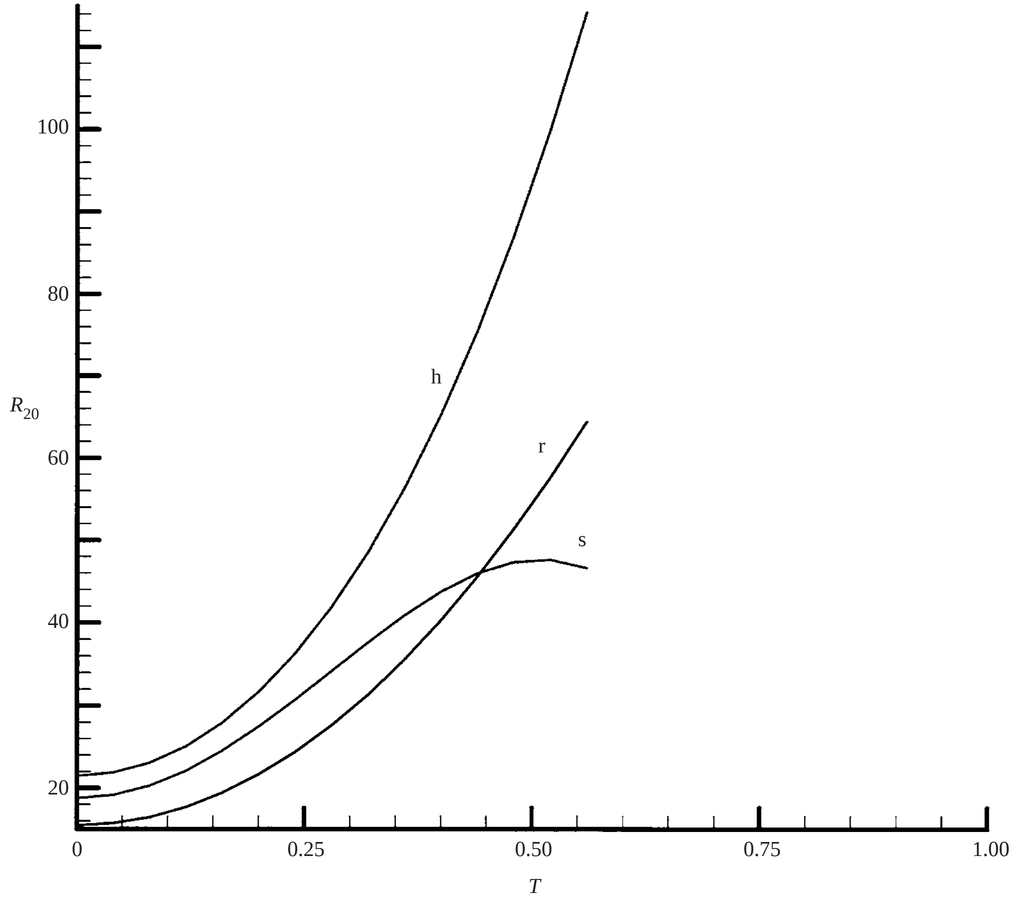

FIGURE 9. R_{20} against $\mathscr{T}$ for rolls (r), squares (s) and hexagons (h). Here $S_t = 1.0$, $C = 1.0$ and $K_2 = 0$.

down-hexagons and up-hexagons are found to be possibly stable in particular range of values for the non-dimensional parameters and for ε. The results are briefly as follows. Supercritical rolls are stable only if

$$|\varepsilon| \geqslant \varepsilon_1, \quad \varepsilon_1 = \frac{\sqrt{3}|R_1|}{R_{20}^{(r)}}, \quad 0 < R_{20}^{(r)} \leqslant R_{20}^{(s)}, \quad 0 < R_{20}^{(r)} \leqslant R_{20}^{(re)}. \tag{34a}$$

Supercritical squares are stable only if

$$|\varepsilon| \geqslant \varepsilon_2, \quad \varepsilon_2 = \frac{\sqrt{3}|R_1|}{\sqrt{2}\left(R_{20}^{(r)} - R_{20}^{(s)}\right)}, \quad R_{20}^{(r)} > R_{20}^{(s)} > 0, \quad R_{20}^{(re)} \geqslant R_{20}^{(s)} > 0. \tag{34b}$$

Supercritical rectangles are stable only if

$$|\varepsilon| \geqslant \varepsilon_3, \quad \varepsilon_3 = \frac{\sqrt{3}|R_1|}{\sqrt{2}\left(R_{20}^{(r)} - R_{20}^{(re)}\right)}, \quad R_{20}^{(r)} > R_{20}^{(re)} > 0, \quad R_{20}^{(s)} \geqslant R_{20}^{(re)} > 0. \tag{34c}$$

Subcritical down-hexagons are stable only if

$$\varepsilon_4 \leqslant |\varepsilon| \leqslant \varepsilon_5, \quad \varepsilon_4 = \frac{|R_1|}{R_{20}^{(h)}}, \quad \varepsilon_5 = \frac{6|R_1|}{R_{20}^{(h)} - R_{20}^{(r)}}, \quad R_1 > 0. \tag{34d}$$

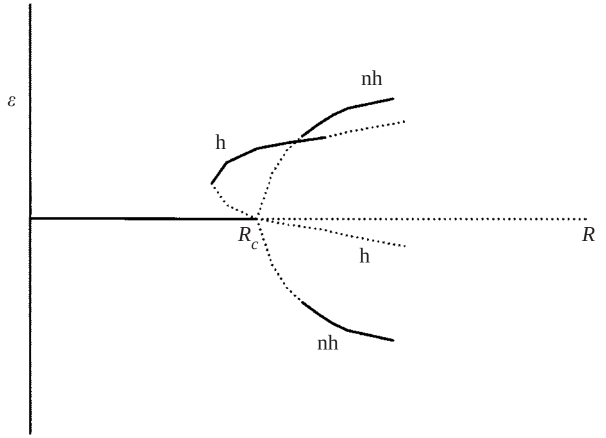

FIGURE 10. Bifurcation diagram in the (R, ε)-plane. Solid and dotted lines represent, respectively, stable and unstable branches. The lines h and nh represent, respectively, hexagons and non-hexagons.

Subcritical up-hexagons are stable only if

$$\varepsilon_4 \leqslant |\varepsilon| \leqslant \varepsilon_5, \quad R_1 < 0. \tag{34e}$$

Figure 10 provides a qualitative bifurcation diagram representing the amplitude ε versus R for those solutions that are possibly stable in particular range of ε according to (34). Solid lines correspond to linearly stable branches while dotted lines correspond to linearly unstable branches. Note that this diagram does not include a three-dimensional solution that is always unstable. This bifurcation diagram shows different cases for possibly stable solutions. For $\mathscr{T} < \mathscr{T}_{c7}$, the two-dimensional roll branch bifurcates supercritically and is initially unstable to a subcritically bifurcating hexagonal branch. The hexagonal branch either is due to up-hexagons if ε is positively upward in the diagram or is due to down-hexagons if ε is positively downward. For $\mathscr{T}_{c7} < \mathscr{T} < \mathscr{T}_{c4}$, the square branch bifurcates supercritically and is initially unstable to a subcritically bifurcating hexagonal branch. For $\mathscr{T}_{c5} < \mathscr{T} < \mathscr{T}_{c6}$, the rectangular branch bifurcates supercritically and is initially unstable to subcritically bifurcating hexagonal branch.

To illustrate (34) and to provide specific stable flow patterns for different values of $\mathscr{T}$, we use (25) and (34) to present briefly the following three examples, for which $K_c = K_2 = 0$ and $S_t = C = 1.0$. The first example is $\mathscr{T} = 0.12$ where (34*a*) and (34*e*) are applicable. For $0.006 \leqslant |\varepsilon| \leqslant 0.115$, up-hexagons are stable, while rolls are stable for $|\varepsilon| \geqslant 0.014$. There is an overlap region $0.014 \leqslant |\varepsilon| \leqslant 0.115$ for which both up-hexagons and rolls are stable and hysteretic effect can occur, where the solution realized can depend on the initial condition. The second example is $\mathscr{T} = 0.20$ where (34*c*) and (34*d*) are applicable. For $0.009 \leqslant |\varepsilon| \leqslant 0.179$, down-hexagons are stable, while rectangles at about $\gamma = 63°$ are stable for $|\varepsilon| \geqslant 0.020$. There is an overlap region $0.020 \leqslant |\varepsilon| \leqslant 0.179$ for which both down-hexagons and such rectangles are stable. The last example is $\mathscr{T} = 0.80$ where (34*b*) and (34*d*) are applicable. For $0.077 \leqslant |\varepsilon| \leqslant 0.923$, down-hexagons are stable, while squares are stable for $|\varepsilon| \geqslant 0.192$. There is an overlap region $0.192 \leqslant |\varepsilon| \leqslant 0.923$ for which both down-hexagons and squares are stable.

5. Conclusion and some remarks

We have investigated the problem of nonlinear steady convection in a rotating mushy layer during alloy solidification, and analysed the two- and three-dimensional steady modes using the model due to Amberg & Homsy (1993). We performed a weakly nonlinear analysis by taking into account all the linear and nonlinear interaction terms, including those between the local solid fraction and the flow associated with the Coriolis term, in the governing equations to determine the steady solutions admitted by the nonlinear problem, and employed stability analysis to determine the solutions that can be stable with respect to arbitrary three-dimensional disturbances in different ranges of the parameter values and the amplitude of motion ε. We found that, depending on the range of values of the parameters and ε, two-dimensional oblique rolls and distorted three-dimensional solutions in the form of squares, rectangles, down-hexagons and up-hexagons are possibly stable. We found that two-dimensional rolls are supercritical and stable only if ε is equal to or above some value ε_1 and $\mathscr{T}$ is below some values $\mathscr{T}_{c5}$ and $\mathscr{T}_{c7}$ or above some values $\mathscr{T}_{c4}$ and $\mathscr{T}_{c6}$. Three-dimensional squares (rectangles) are stable only if they are supercritical, ε is equal to or above some value ε_2 (ε_3) and $\mathscr{T}$ lies in the range $\mathscr{T}_{c7} < \mathscr{T} < \mathscr{T}_{c4}$ ($\mathscr{T}_{c5} < \mathscr{T} < \mathscr{T}_{c6}$). Subcritical squares and subcritical rectangles also can exist but they are unstable. Subcritical down-hexagons are stable only if ε lies in the range $\varepsilon_4 \leqslant \varepsilon \leqslant \varepsilon_5$ and $R_1 > 0$. Subcritical up-hexagons are stable only if ε lies in the range $\varepsilon_4 \leqslant \varepsilon \leqslant \varepsilon_5$ and $R_1 < 0$. Supercritical down-hexagons and supercritical up-hexagons also can exist but they are unstable. There are certain overlap regions in ε where more than one solution can be stable and, thus, there can be a hysteretic effect in such overlap regions. The results of our studies on the onset of plume convection and chimney formation within the mushy layer indicated that they are most likely to be initiated near the lower boundary of the layer. The presence of rotation was found to reduce the tendency for chimney formation at the centres of rolls and at the nodes on the boundaries of hexagons. The stability of supercritical rectangles and squares uncovered in the present study was found to be entirely due to the interactions between the local solid fraction and the Coriolis term in the momentum-Darcy equation, and such interactions were also found to enhance significantly the stability of the subcritical down-hexagons.

As mentioned in § 1, Guba (2001) studied the problem of finite-amplitude steady convection in a rotating mushy layer without taking into account interactions between the local solid fraction and the Coriolis term. Guba carried out a weakly nonlinear analysis of two-dimensional oblique rolls and distorted hexagons, by calculating only the leading non-zero coefficient beyond R_c in the expansion for R for each solution, but made no stability analysis of these finite-amplitude solutions. Similarly to Amberg & Homsy (1993), Guba (2001) studied the case where the permeability coefficient K_1 can be in general an order-one quantity and predicted, like Amberg & Homsy (2001), that depending on the range of the parameter values, either subcritical or supercritical rolls can exist, and subcritical hexagons can change their form from up-hexagons to down-hexagons for $\mathscr{T}$ beyond some critical value. It should, however, be noted that one can show that such subcritical rolls as well as the hexagonal solutions found by Guba are unstable. Also, as was shown in the present study, the supercritical rolls found by Guba cannot be realizable over certain range of values of $\mathscr{T}$ if the interaction terms between the local solid fraction and the Coriolis term are taken into account. Guba's results were reported for $\mathscr{T}$ as large as 7. However, as was found in the present study, if the interaction between the local solid fraction and the Coriolis term is taken into account, then the validity of the results for $\mathscr{T} > 1$ is questionable since $|R_1|$ and $|R_{20}|$ can become much larger than unity, by about 2 to 3 orders of magnitude, for $\mathscr{T}$ just above unity, so that expansions of the type (8), which assumes that the coefficients, such as $|R_1|$ and $|R_{20}|$, in those double-expansions in powers of ε and δ be of order unity, can no longer be justified.

As already noted, we were interested in carrying out a significant extension of the work by Guba (2001) by fully including the interaction between the local solid fraction and the Coriolis term, carrying out a weakly nonlinear analysis to determine all the two- and three-dimensional steady solutions admitted by the nonlinear system and performing stability analyses of the finite-amplitude solutions to determine all the possible stable solutions. During our extensive investigation, we were able to uncover significant new results and new flow features that can increase our understanding of the effects of the external constraint of rotation on the flow in mushy layers, which hopefully could aid future studies in the area. When comparing the present results to some experimental results, it should be noted that all the available experimental results, which are due to Sample & Hellawell (1982, 1984) and Claben, Heimpel & Christensen (1999), have been for fully nonlinear convection with fully developed chimneys, and thus are not applicable to the present results for weakly nonlinear convection near the onset of motion. It is hoped that some experimental studies of the present problem could be carried out in the near future for a comparison with the present qualitative results. As was shown by Guba (2001), the case $\mathscr{T} \leqslant 1$ can be quite accessible in the laboratory for an ammonium chloride–water system since it yields a value of the rotation rate about $\omega \leqslant 2.0$ rad s^{-1}.

REFERENCES

Amberg, G. & Homsy, G. M. 1993 Nonlinear analysis of buoyant convection in binary solidification with application to channel formation. *J. Fluid Mech.* **252**, 79–98.

Anderson, D. M. & Worster, M. G. 1995 Weakly nonlinear analysis of convection in mushy layers during the solidification of binary alloys. *J. Fluid Mech.* **302**, 307–331.

Busse, F. H. 1967 The stability of finite-amplitude convection and its relation to an extremum principal. *J. Fluid Mech.* **30**, 625–649.

Busse, F. H. 1989 Fundamentals of thermal convection. In *Mantle Convection, Plate Tectonics and Global Dynamics* (ed. W. R. Peltier), pp. 23–95. Gordon and Breach.

Busse, F. H. & Riahi, D. N. 1980 Nonlinear convection in a layer with nearly insulating boundaries. *J. Fluid Mech.* **96**, 243–256.

Chandrasekhar, S. 1961 *Hydrodynamic and Hydromagnetic Stability*. Clarendon.

Claben, S., Heimple, M. & Christense, U. 1999 Blob instability in rotating compositional convection. *Geophys. Res. Lett.* **26**, 135–138.

Fowler, A. C. 1985 The formation of freckles in binary alloys. *IMA J. Appl. Maths* **35**, 159–174.

Gorkov, L. P. 1957 Stationary convection in a plane liquid near the critical heat transfer point. *Sov. Phys. JETP* **6**, 311–315.

Govender, S. & Vadasz, P. 2002 Weak non-linear analysis of moderate Stefan number stationary convection in rotating mushy layers. *Transport in Porous Media* **49**, 247–263.

Guba, P. 2001 On the finite-amplitude steady convection in rotating mushy layers. *J. Fluid Mech.* **437**, 337–365.

Neilson, D. G. & Incropera, F. P. 1993 Effect of rotation on fluid motion and channel formation during unidirectional solidification of a binary alloy. *Intl J. Heat Mass Transfer* **36**, 489–505.

Nield, D. A. 1998 Instability and turbulence in convective flows in porous media. In *Nonlinear Instability, Chaos and Turbulence* (ed. L. Debnath & D. N. Riahi), Vol. 1, pp. 225–276. WIT.

Riahi, D. N. 1993 Effect of rotation on the stability of the melt during the solidification of a binary alloy. *Acta Mechanica* **99**, 95–101.

SAMPLE, A. K. & HELLAWELL, A. 1982 The effect of mold precession on channel and macro-segregation in ammonium chloride-water analog casting. *Metall. Trans.* B **13**, 495–501.

SAMPLE, A. K. & HELLAWELL, A. 1984 The mechanisms of formation and prevention of channel segregation during alloy solidification. *Metall. Trans.* A **15**, 2163–2173.

SCHLUTER, A., LORTZ, D. & BUSSE, F. H. 1965 On the stability of finite amplitude convection. *J. Fluid Mech.* **23**, 129–144.

TAIT, S., JAHRLING, K. & JAUPART, C. 1992 The planform of compositional convection and chimney formation in a mushy layer. *Nature* **359**, 406–408.

VERONIS, G. 1959 Cellular convection with finite amplitude in a rotating fluid. *J. Fluid Mech.* **5**, 401–435.

WORSTER, M. G. 1992 Instabilities of the liquid and mushy regions during solidification of alloys. *J. Fluid Mech.* **237**, 649–669.